Kawase *et al. Earth, Planets and Space* (2018) 70:1
https://doi.org/10.1186/s40623-017-0766-4

Earth, Planets and Space

FULL PAPER

Open Access

Difference of horizontal-to-vertical spectral ratios of observed earthquakes and microtremors and its application to S-wave velocity inversion based on the diffuse field concept

Hiroshi Kawase[1*], Yuta Mori[2] and Fumiaki Nagashima[1]

Abstract

We have been discussing the validity of using the horizontal-to-vertical spectral ratios (HVRs) as a substitute for S-wave amplifications after Nakamura first proposed the idea in 1989. So far a formula for HVRs had not been derived that fully utilized their physical characteristics until a recent proposal based on the diffuse field concept. There is another source of confusion that comes from the mixed use of HVRs from earthquake and microtremors, although their wave fields are hardly the same. In this study, we compared HVRs from observed microtremors (MHVR) and those from observed earthquake motions (EHVR) at one hundred K-NET and KiK-net stations. We found that MHVR and EHVR share similarities, especially until their first peak frequency, but have significant differences in the higher frequency range. This is because microtremors mainly consist of surface waves so that peaks associated with higher modes would not be prominent, while seismic motions mainly consist of upwardly propagating plain body waves so that higher mode resonances can be seen in high frequency. We defined here the spectral amplitude ratio between them as EMR and calculated their average. We categorize all the sites into five bins by their fundamental peak frequencies in MHVR. Once we obtained EMRs for five categories, we back-calculated EHVRs from MHVRs, which we call pseudo-EHVRs (pEHVR). We found that pEHVR is much closer to EHVR than MHVR. Then we use our inversion code to invert the one-dimensional S-wave velocity structures from EHVRs based on the diffuse field concept. We also applied the same code to pEHVRs and MHVRs for comparison. We found that pEHVRs yield velocity structures much closer to those by EHVRs than those by MHVRs. This is natural since what we have done up to here is circular except for the average operation in EMRs. Finally, we showed independent examples of data not used in the EMR calculation, where better ground structures were successfully identified from pEHVRs again. Thus we proposed here a simple empirical method to estimate S-wave velocity structures using single-station microtremor records, which is the most cost-effective method to characterize the site effects.

Keywords: Site effect, Subsurface structure, Seismological bedrock, Horizontal-to-vertical ratio, Hybrid heuristic search, S-wave, P-wave

*Correspondence: kawase@zeisei.dpri.kyoto-u.ac.jp
[1] DPRI, Kyoto University, Gokasho, Uji, Japan
Full list of author information is available at the end of the article

Introduction

It is essential to evaluate the subsurface structure properly and validate previously proposed structures based on geological data and boring explorations with the observed seismic and non-seismic data for the quantitative prediction of ground motions in urban areas. There are plenty of methods to evaluate subsurface structures that may reproduce observed site characteristics of observed ground motions. However, there are not so many methods that can reliably determine S-wave velocity structures down to the seismological bedrock, where the S-wave velocity reaches 3.0 km/s or higher. Array measurements of microtremors to obtain phase velocities of propagating surface waves (e.g., Horike 1985; Okada 2003) have been successfully utilized to invert S-wave velocity structures down to the seismological bedrock for more than three decades. Several applications of the method at different sites (e.g., Picozzi et al. 2009; Prieto et al. 2009; Stephenson et al. 2009) show the robustness of the method under various environments. Recent advances by Cho et al. (2006) and Tada et al. (2007) as a natural extension of the pioneering work of the so-called SPAC method by Aki (1957) provide us quite a strong tool for dispersion analysis. The downside of these array methods is that we need to deploy as many stations as possible for the precise determination of phase velocity at one frequency band and the array size must be increased in proportion to the targeted depth. As the array size is increased, the fundamental assumption of horizontally homogeneous layering would be difficult to expect. Also these array methods need very low-noise sensors with high coherence, especially in the long period range.

The spectral ratio approach with a reference site for seismic motions, either on the surface or inside the borehole, can be quite effective for obtaining a reliable S-wave velocity structure when combined with a standard inversion technique such as genetic algorithm or simulated annealing. However, the spectral ratio approach with respect to the rock outcrop reference site, sometimes called the standard spectral ratio (SSR) method, will fail to provide reasonable site amplification either when the reference site is not sufficiently close to the target site or when the reference site is not close the seismological bedrock in terms of its S-wave velocity. The so-called generalized spectral inversion method (Andrews 1986) will provide better site amplification characteristics if we find a good reference site among stations used because the generalized inversion makes use of all the data at once with proper attenuation correction and so the distance between the reference site and the target site is not an issue. Also once the inversion analysis is done, we can select the best site for reference, that is, the smallest amplification site with flat frequency dependence. In Kawase and Matsuo (2004) and following Nakano et al. (2015), the site amplification factors for K-NET, KiK-net, and the JMA Shindokei network relative to the seismological bedrock outcrop at the reference site (YMGH01) were obtained and then used to invert S-wave velocity structures at these sites.

As for the surface-to-borehole spectral ratio method, there is no problem for distance since the horizontal location of two sensors should be close together in a horizontal space. However, it is also quite a common situation to have a reference site not close to the seismological bedrock depth, especially for deep sedimentary basin sites. Even if the borehole station were well within a seismological bedrock formation, the surface-to-borehole spectral ratio is contaminated by the reflected phase at the free surface (e.g., Steidl et al. 1996; Satoh et al. 1997), which sometimes makes frequencies and amplitudes of peaks unstable for different clusters of sources.

Recently, using the cross-correlation of two stations the so-called Green's function retrieval method based on the diffuse field concept (DFC) is commonly applied to both seismic data and long-duration of microtremor data (e.g., Campillo and Paul 2003). The dispersion characteristics of the obtained Green's functions can be used to determine the averaged S-wave velocity structure between two stations. This is quite a powerful method to determine a velocity structure averaged over the whole path between two stations; however, it does not provide a velocity structure immediately below the observed site. Besides, it may need to measure microtremors for sufficiently long duration (from several weeks to months) to get stable results.

After successful application of the cross-correlation analysis of earthquake and microtremor data, it is natural to make two stations coincide with each other, that is, to utilize the auto-correlation of a single-station measurement. In the auto-correlation approach, we can determine the velocity structure immediately below the observed site because of the direct correspondence of the imaginary part of the Green's function to the spectral energy density (Sánchez-Sesma et al. 2011). As a pioneering work, Margerin et al. (2009) showed that after sufficient lapse time from the onset of the S-wave the late coda can be considered to be in the diffuse field regime. Then, Kawase et al. (2011) extended the idea of DFC to the stack of horizontal-to-vertical ratios of earthquakes (EHVR) and provided a simple theoretical formula assuming equipartition of energy in the incident waves at the bedrock (i.e., equipartition inside the half-space). It turned out that this is a powerful tool to determine the S-wave velocity structure below the observed site of earthquakes down to the seismological bedrock, as evidenced by Ducellier et al. (2013), Nagashima et al. (2014, 2017) and Fukihara et al. (2015).

Well before the advent of the application of DFC to EHVRs as mentioned above, Sánchez-Sesma et al. (2011) applied the concept to the horizontal-to-vertical ratios of microtremors (MHVR) to derive a formula with horizontal and vertical Green's functions of a point force on the surface. This theoretical formula provides the final solution for the long-lasting debate on the interpretation of MHVR (e.g., Bard 1999; Bonnefoy-Claudet et al. 2004) that began from the initial proposal by Nakamura (1989). The DFC theory for MHVR can be used for the velocity structure inversion. The validation studies of this DFC interpretation of MHVR can be found in Salinas et al. (2014), Kawase et al. (2015), and Lontsi et al. (2015). Recently García-Jerez et al. (2016) show a new calculation scheme using residue integrals, which is much more efficient in computing Green's functions and so they used it for velocity inversion.

Even though the calculation method for MHVR implemented by García-Jerez et al. (2016) is more efficient than the ordinary wavenumber integration scheme, still it is quite time-consuming because of the inevitable summation to account for multiple contributions of poles in the wavenumber domain. On the other hand, the theory for EHVR is easy to calculate because we need to consider body wave contributions only in one wavenumber. Therefore, the inversion for EHVR is much more efficient than that for MHVR. However, in terms of field measurement effort, a temporal single-station deployment of microtremor measurements for MHVR is much easier and less costly than a long-lasting deployment of seismic motions for EHVR.

That is why we have proposed here a new method in which empirical translation from MHVR to EHVR is performed based on the observed spectral ratio between EHVR and MHVR at the same site, which is called EMR. EMRs are calculated as the averaged values from observed data for different categories classified based on their peak MHVR frequencies. The resultant HVRs, called pseudo-EHVRs or pEHVR here, show quite similar characteristics to the observed EHVRs and so the inverted structures from pEHVRs are also quite similar to those from the observed EHVRs.

Method and data

Earthquake data

After the 1995 Hyogo-ken Nanbu (Kobe) earthquake, several nation-wide strong ground motion observation networks have been deployed, and data from K-NET (Kinoshita 1998) and KiK-net (Aoi et al. 2000; Okada et al. 2004) were used here. These are operated and distributed by the National Research Institute for Earth Science and Disaster Resilience (NIED). Among these K-NET and KiK-net measurement sites, which are around 1700 sites in total, we observed microtremors (ambient noises) at 100 sites by our own efforts from 2000 to 2015. The locations of the sites considered in this study are shown in Fig. 1 and tabulated as Table 1. In Table 1, the earthquake event information, namely hypocentral distance ranges and numbers of event at each site, is added. There are no specific reasons to select these sites.

Measured earthquake records are analyzed according to the calculation flow here. First we select the earthquake data from the database provided by NIED, which contains source information determined by the Japan Meteorological Agency (JMA). Then, we cut out an S-wave record section from the observed data file based on the S-wave onset calculated from JMA source information and JMA's travel time table (the so-called JMA2001 table, JMA 2001). The duration of the section is fixed to be 40.96 s. We also cut out another successive 40.96 s record section as a coda part to compare its spectral characteristics to the S-wave part. After the extraction of these two record sections, we calculate their Fourier spectra and then take a spectral ratio of root-mean-square (RMS) values of two horizontal components with respect to the vertical component to obtain the earthquake horizontal-to-vertical ratio (EHVR hereafter). Once all the records are analyzed, then we calculate the average of all the EHVRs to obtain the average and the average $\pm$ one standard deviations. The average operation here is not the one that the theory of the diffuse field suggests (Sánchez-Sesma et al. 2011; Kawase et al. 2011), in which the average of the normalized spectra for each component should be calculated first and then a ratio between horizontal and vertical components are taken. The reason why we calculate the ratio first is because we would like to check the range of variation of EHVRs for different earthquakes. We confirmed that the averaged EHVRs for these two different ways of calculation are almost the same to each other.

In this research, we analyzed earthquake motions of peak ground acceleration (PGA) from 1.0 to 50.0 cm/s^2 (0.01 m/s^2) among measured earthquake records. This is because the S-wave may not be clear in seismic motion records if PGA is less than 1.0 cm/s^2 and earthquake records exceeding 50.0 cm/s^2 may show nonlinear behavior of the underground structure. Moreover, seismic motions of earthquakes exceeding the JMA magnitude M_{JMA} 6.5 are excluded from analysis to remove earthquake records with significant long period contribution through the excitation of basin-induced or basin-transduced surface waves, since our simple theoretical EHVR formula is derived by considering only body waves.

The portion before arrival of the P-wave is considered as a noise part, up to 40.96 s after the S-wave onset as an S-wave part, and 40.96 s following the S-wave part as a

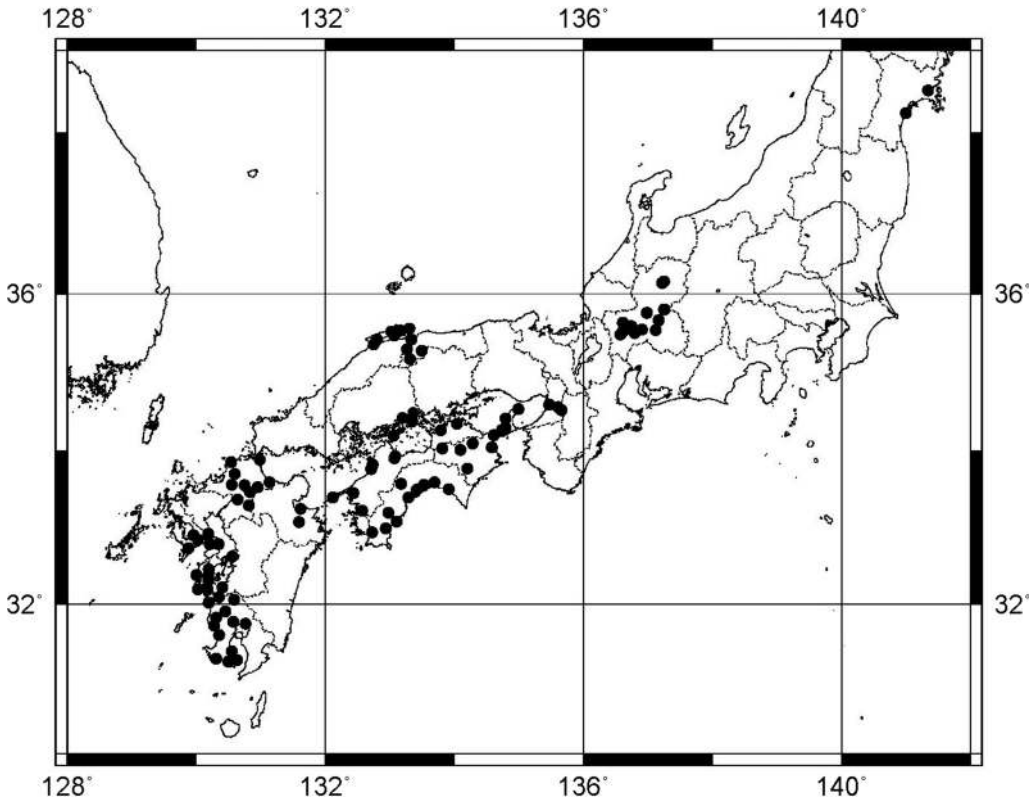

Fig. 1 Location of measurement points

coda part as mentioned before. The measured waveform at one of the K-NET sites, EHM012, is shown in Fig. 2 as an example. Data with length less than 40.96 s are padded with zeros at the end. Spectrum analysis is carried out both in S-wave and coda parts, as well as the noise part to check a signal-to-noise ratio. A cosine-shaped taper is added to both ends before the fast Fourier transform (FFT). Its length is set to be 10% of the data length for the noise part and 2.0 s for the S-wave and coda parts. For K-NET data, Fujiwara et al. (2007) showed that both old instruments until 2002–2006 (K-NET95 type) and replaced instruments after that (K-NET02 type) have flat response up to 30 Hz. Since the sampling rate of KiK-net stations is 200 Hz, we can also expect flat response at least up to 30 Hz.

The time history waveform of three components, namely north–south (NS), east–west (EW), and up–down (UD), are transformed into the frequency domain by FFT. Spectra of earthquakes where the signal-to-noise ratio (SNR) is 2 or more are used to calculate average EHVR. Before taking the ratios, three components of the Fourier spectra are smoothed using a 0.1-Hz Parzen window. We have confirmed the stability of the averaged amplitude irrespective of the choice of the bandwidth from 0.0 to 0.3 Hz.

The individual spectral ratios of NS/UD and EW/UD showed a good match as a whole, although there are a couple of sites that showed a difference more than twice (or half) around the first peak frequency. This kind of directional dependence suggests the effect of 2D/3D surface topography or irregularity in the basin structure (Matsushima et al. 2014). Since we are taking the RMS horizontal amplitude to obtain EHVR, the influence of the directional dependence would be minimal. Figure 3 shows the EHVRs of each observed earthquake and the average EHVR at EHM012 as an example. The black lines are the individual EHVRs (RMS/UD) of earthquakes and the red line is their average (orange lines: average ± one standard deviation). We can see that the EHVRs of individual earthquakes share a common shape, and the average EHVRs of both the S-wave part and the coda part are quite similar to each other. The latter phenomenon was already reported in Satoh et al. (2001) for about ten sites in the Sendai basin. It should be noted, however, the deviation from earthquake to earthquake is larger in the coda part, especially in the low-frequency range. The coda part is considered to be stable in amplitude because of multiple scattering with different directions of arrival, but the S-wave part is found to be as stable as or more

Table 1 List of measurement points and event information used

Code	Longitude (E)	Latitude (N)	Hypocentral distance range (km)			No. of events	Code	Longitude (E)	Lattitude (N)	Hypocentral distance range (km)			No. of events
			Minimum	Average	Maximum					Minimum	Average	Maximum	
EHM003	133.0843	33.9266	60.8	86.4	139.5	18	KGS020	130.4915	31.2396	7.9	113.6	271.1	50
EHM008	132.7282	33.8198	41.1	91.4	205.3	39	KGS021	130.6324	31.2535	8.4	89.5	170.3	12
EHM011	132.4336	33.4496	37.8	91.1	246.6	49	KGW003	133.7896	34.2652	30.1	105.2	290.6	26
EHM012	132.5727	33.2217	28.2	94.2	250.1	50	KGW004	134.0374	34.3473	36.6	94.1	231.2	26
EHM013	132.1141	33.3924	34.8	71.3	142.9	36	KMM015	130.4046	32.2161	17.9	69.0	228.8	30
EHM016	132.7089	33.7654	40.1	84.0	209.1	34	KMM019	130.1938	32.4589	22.9	66.7	223.6	17
EHMH04	133.0658	33.9023	42.8	83.4	172.9	21	KMM020	130.1807	32.3636	34.1	45.0	66.5	20
EHMH10	133.0581	34.1918	15.7	95.4	204.9	71	KMM021	129.9997	32.3793	36.6	77.4	242.0	24
FKOH01	130.9798	33.8849	15.2	89.9	183.0	63	KMM022	130.0265	32.1945	22.5	52.3	97.0	22
FKOH02	130.5963	33.6963	19.0	73.9	205.0	4	KMMH07	130.5584	32.6234	15.4	63.7	264.2	67
FKOH03	130.5499	33.5608	16.6	49.9	213.2	106	KMMH10	130.1811	32.3151	23.1	90.7	312.8	24
FKOH04	130.7451	33.5512	15.4	64.8	196.9	85	KOC003	133.9068	33.5014	18.3	80.2	274.9	17
FKOH05	130.9503	33.5293	20.4	69.3	180.7	89	KOC005	133.6921	33.5934	4.5	71.9	184.6	16
FKOH06	131.1348	33.5925	33.4	78.7	188.1	75	KOC006	133.4165	33.4945	20.7	94.6	238.0	22
FKOH07	130.6354	33.3678	14.0	72.6	213.7	33	KOC007	133.5271	33.5611	14.6	91.1	247.3	18
FKOH08	130.8285	33.4654	11.6	76.4	193.4	120	KOC009	133.1718	33.5742	44.6	97.6	222.5	29
FKOH09	130.5432	33.8501	18.0	43.4	206.1	95	KOC010	133.2896	33.3925	40.2	95.9	227.3	25
FKOH10	130.8170	33.2891	15.9	61.0	232.5	62	KOC012	132.9758	33.1967	48.6	96.2	204.3	36
GIF005	137.2514	36.1536	19.2	52.1	191.1	54	KOC013	133.1015	33.0797	59.2	115.7	291.5	34
GIF010	137.2450	35.8029	11.9	62.3	171.4	62	KOC014	132.9377	32.9895	44.4	105.9	267.6	26
GIF011	136.9808	35.7593	15.0	69.6	177.0	58	KOC015	132.7252	32.9370	33.1	105.2	255.7	53
GIF013	137.1617	35.6637	8.9	65.7	157.7	41	MYGH01	140.9969	38.2400	22.5	107.5	306.6	112
GIF015	136.9072	35.5454	24.3	75.7	169.3	36	MYGH11	141.3421	38.5158	16.4	103.3	308.0	81
GIF016	137.1191	35.5424	14.5	66.4	153.0	38	NGS008	130.1843	32.9231	20.3	59.9	97.7	9
GIF017	136.5714	35.4829	29.2	84.4	265.4	39	NGS009	130.0218	32.8456	14.2	68.6	103.7	22
GIF026	136.7414	35.5912	35.1	82.8	273.1	66	NGS010	129.8763	32.7353	14.9	75.1	114.2	26
GIFH03	136.6134	35.6325	14.3	92.9	489.5	104	NGS011	130.2024	32.7839	46.8	66.4	100.8	8
GIFH06	136.7939	35.5038	9.6	87.3	498.5	52	NGS012	130.3463	32.7884	18.0	87.5	268.5	25
GIFH15	137.2208	36.1338	13.8	76.4	327.8	143	NGS019	129.9582	32.9002	12.4	66.8	214.9	16
GIFH20	137.2531	35.7991	11.5	67.1	549.1	162	OIT010	131.6103	33.2478	15.3	75.4	146.6	17
GIFH25	136.6127	35.5214	15.6	83.3	484.4	101	OIT013	131.5934	33.0726	28.9	107.6	302.9	56
HRS015	133.3615	34.4849	61.8	77.9	114.2	10	OSK006	135.4710	34.5894	34.1	71.2	96.1	11
HRS016	133.1971	34.4198	21.4	83.0	260.9	16	OSK007	135.6058	34.5577	28.2	91.4	275.9	27

Table 1 continued

Code	Longitude (E)	Latitude (N)	Hypocentral distance range (km)			No. of events	Code	Longitude (E)	Lattitude (N)	Hypocentral distance range (km)			No. of events
			Minimum	Average	Maximum					Minimum	Average	Maximum	
HRSH04	133.3493	34.3785	21.2	86.7	267.6	26	OSKH03	135.6608	34.5248	13.1	92.6	280.3	14
HYG024	134.9904	34.5330	20.1	71.5	262.1	34	SMN002	133.0682	35.4714	25.2	68.5	238.7	17
HYG026	134.7925	34.4149	12.5	83.7	290.1	42	SMN005	132.7449	35.3611	19.4	72.4	217.8	14
HYG027	134.7292	34.2499	22.7	67.5	193.7	17	SMN020	133.1652	35.5347	67.2	94.7	248.6	4
HYGH01	134.7941	34.2937	16.6	90.3	366.7	33	SMNH01	133.2604	35.2963	9.2	50.4	231.9	34
KGS001	130.1763	32.1947	25.2	60.5	244.0	26	SMNH10	133.3004	35.5579	19.7	72.2	248.4	13
KGS002	130.3519	32.0916	16.1	41.2	211.9	22	SMNH11	132.8008	35.4259	25.5	80.5	319.0	15
KGS003	130.5874	32.0559	17.1	88.6	307.0	44	SMNH15	133.0226	35.5232	22.1	45.5	103.1	7
KGS004	130.1927	32.0145	13.6	58.4	257.3	29	TKS001	134.6098	34.2030	24.8	77.6	269.0	29
KGS005	130.4513	31.9006	9.6	79.0	220.2	26	TKS002	134.5820	34.0438	13.2	76.5	180.7	14
KGS007	130.3032	31.8143	18.4	65.7	183.5	21	TKS007	134.2850	34.0905	43.5	92.7	238.7	14
KGS008	130.5699	31.7621	26.9	85.1	225.9	30	TKS009	134.1995	33.7719	30.5	78.6	303.3	21
KGS009	130.7613	31.7368	11.9	88.1	325.6	58	TKS012	133.8090	34.0319	15.1	94.8	281.9	15
KGS010	130.2735	31.7123	27.3	82.4	241.0	31	TKSH02	134.0918	34.0112	14.6	94.3	312.2	47
KGS011	130.3490	31.5896	39.6	80.3	162.3	18	TTR007	133.4876	35.2826	15.4	71.0	337.5	30
KGS018	130.5449	31.3757	12.4	118.4	297.5	69	TTR008	133.3301	35.4258	13.8	56.8	177.5	15
KGS019	130.3008	31.2776	22.3	97.4	249.7	27	TTR009	133.3113	35.1708	12.7	60.6	319.8	28

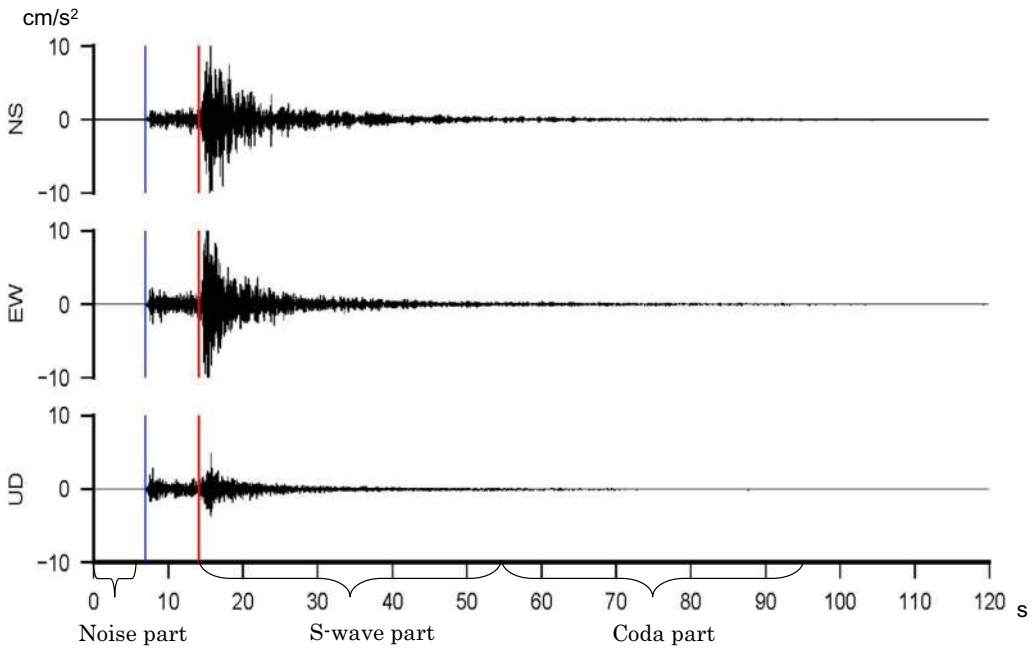

Fig. 2 Example of a measured earthquake waveform at EHM012 and sections of noise, S-wave, and coda parts

stable than the coda part in terms of the HVRs. Please note that the coda part here is just a successive section of record immediately after the S-wave part with the same durations of 40.96 s and no dependence with respect to the source–site distance or the S–P time is considered as is usually adopted in the coda study.

Microtremor data

Microtremor observation at K-NET and KiK-net sites was done by using an SMAR-6A3P equipped with three component moving-coil type accelerometers with low-noise amplifiers from Mitutoyo Corporation, in which the data logger was replaced by LS8800 with 24-bit A/D converters from Hakusan Corporation. The data sampling is set to be 100 Hz. Typically, measurement was done in a day time with the duration of 15–20 min at one site (30 min at a noisy site).

Measured microtremor records are analyzed according to the calculation flow here. First the whole continuously observed records with 900–1200 s in duration are subdivided into record sections of 40.96 s by overlapping 50%. We make a list of all the record sections in descending order based on the three components RMS amplitudes and then see its short-time average (STA)/long-time average (LTA) ratio for the first best 15 segments. If the STA/LTA ratio is significantly larger than the other segments selected, we discard that segment and choose another segment (with slightly higher RMS amplitude) on the list until we select 15 segments. Then we visually inspected these 15 waveforms and if we found a segment or segments with some significant time-varying noises, we discarded and replace it by another better segment from the list. Figure 4 shows the measured microtremor waveform and sections used at the same site for earthquake example, EHM012.

As is the earthquake data analysis, three components are used to analyze, two horizontal components of which are used to calculate their RMS value. Then microtremor HVR (hereafter MHVR) is calculated as a ratio of RMS/UD. Finally, the MHVRs calculated for each segment are averaged over fifteen segments. Smoothing on the Fourier spectra is obtained by a 0.1-Hz Parzen window as is the earthquake data analysis. Also a cosine taper of 2.0 s is added to both ends of the time history before FFT.

There is not much difference between the NS/UD and EW/UD of each site, as is the case of earthquake motions. Figure 5 shows the MHVRs of individual segments (RMS component, black lines), the averaged MHVR (red line), and the average ± one standard deviation (orange line) at the site EHM012 as an example. As is well known, the MHVRs are quite stable with time.

Velocity inversion using the theory for EHVR

Since we are applying the same inversion procedure developed for the EHVR by Nagashima et al. (2014, 2017), we only briefly describe the basic explanation of the assumptions and the method used.

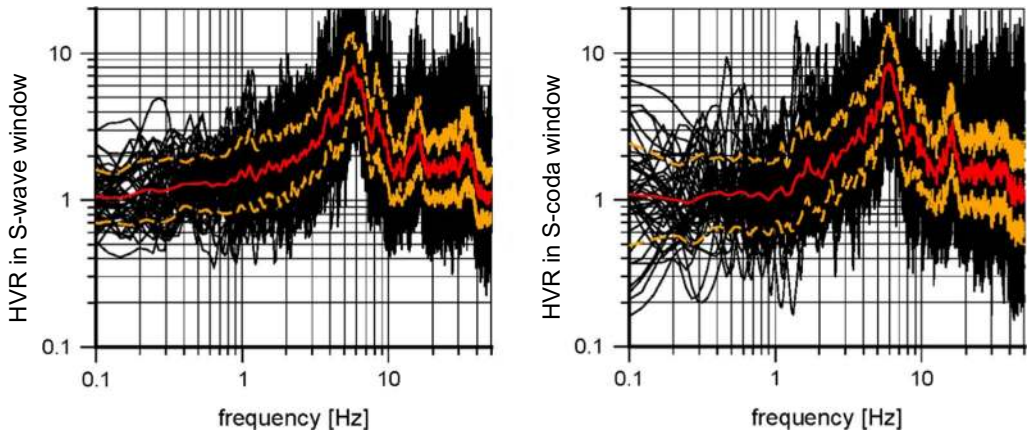

Fig. 3 Measured EHVR at a measurement point EHM012. The averaged EHVR (red), average ± one standard deviation (orange), and individual EHVRs (black). Left: S-wave part, right: coda part immediately after S-wave part

First we summarized basic formulas to calculate the theoretical EHVR based on DFC. Under the assumption of DFC and subsequent energy-equipartitioned condition, we can show that the diffused-wave energy spectra $E(P, \omega)$ at position P would be proportional to the normalized auto-correlation of observed displacement $|u(P, \omega)|^2$, which in turn would be proportional to the imaginary part of the Green's function at P as

$$E(P,\omega) \propto \left\langle \frac{|u(P,\omega)|^2}{\int |u(P,\varpi)|^2 \mathrm{d}\varpi} \right\rangle \propto \mathrm{Im}(G(P,P,\omega)) \tag{1}$$

For EHVR coming from a far-field source, following Claerbout (1968), we can write

$$\begin{aligned} \left\langle \frac{|u(P,\omega)|^2}{\int |u(P,\varpi)|^2 \mathrm{d}\varpi} \right\rangle &= K \times |\mathrm{TF}(\omega)|^2 \\ &= -K \times \rho_\mathrm{H} c_\mathrm{H} \omega \mathrm{Im}[G^\mathrm{Eq}(P,P,\omega)] \end{aligned} \tag{2}$$

where $\rho_\mathrm{H} c_\mathrm{H}$ is the impedance of the half-space and $\mathrm{TF}(\omega)$ is the transfer function of the corresponding body wave. Therefore, we can get a simple formula for the surface observation of seismic motions as

$$\begin{aligned} \frac{H(0,\omega)}{V(0,\omega)} &= \sqrt{\frac{\mathrm{Im}[G^\mathrm{Eq}_\mathrm{horizontal}(0,0;\omega)]}{\mathrm{Im}[G^\mathrm{Eq}_\mathrm{vertical}(0,0;\omega)]}} \\ &= \sqrt{\frac{\alpha_\mathrm{H}}{\beta_\mathrm{H}}} \frac{|\mathrm{TF}_\mathrm{horizontal}(0,\omega)|}{|\mathrm{TF}_\mathrm{vertical}(0,\omega)|} \end{aligned} \tag{3}$$

where α_H and β_H are the P- and S-wave velocities of the half-space, respectively. In this case, one-directional HVR (i.e., NS/UD and EW/UD) calculation is assumed (e.g., Matsushima et al. 2014).

EHVR inversion

The inversion scheme used here is basically the same as those proposed by Nagashima et al. (2014, 2017), who extensively studied the velocity structures at the MYG004K-NET site and its neighboring areas using a temporary deployment of aftershock observation for the 2011 Tohoku earthquake. For the inversion of S-wave velocity structures, they used the scheme proposed by Yamanaka (2007), the so-called hybrid heuristic search (HHS) method. The method does not require an initial model, but it would be better to have one to constrain the searching range of parameters. For K-NET sites we have S-wave velocity information of downhole P- and S-wave logging down to 20 m at most, while for KiK-net sites we have them down to the borehole sensor depths, typically 100–200 m. In the S-wave velocity inversion using EHVRs, we need to determine P- and S-wave velocities down to the seismological bedrock whose S-wave velocity would be more than 3 km/s, as shown in Eq. (3). This makes possible to use not only peak frequencies but also their amplitude to reproduce observed EHVRs. For deep basin structures at K-NET and KiK-net sites, we can refer to the J-SHIS model of the shallow (< 10 km) crust, which can be downloaded from the portal site of J-SHIS (http://www.j-shis.bosai.go.jp/en/, last accessed on 2017/01/28). P-wave velocities are not the target of inversion but translated from the inverted S-waves based on the empirical relationship. We assume 1.1% damping for all the layers.

The residual (misfit) function to optimize is shown in Eq. (4), where the residual is normalized by the frequency f because equal sampling in frequency from FFT makes relatively increased numbers of constraint in the higher frequency range

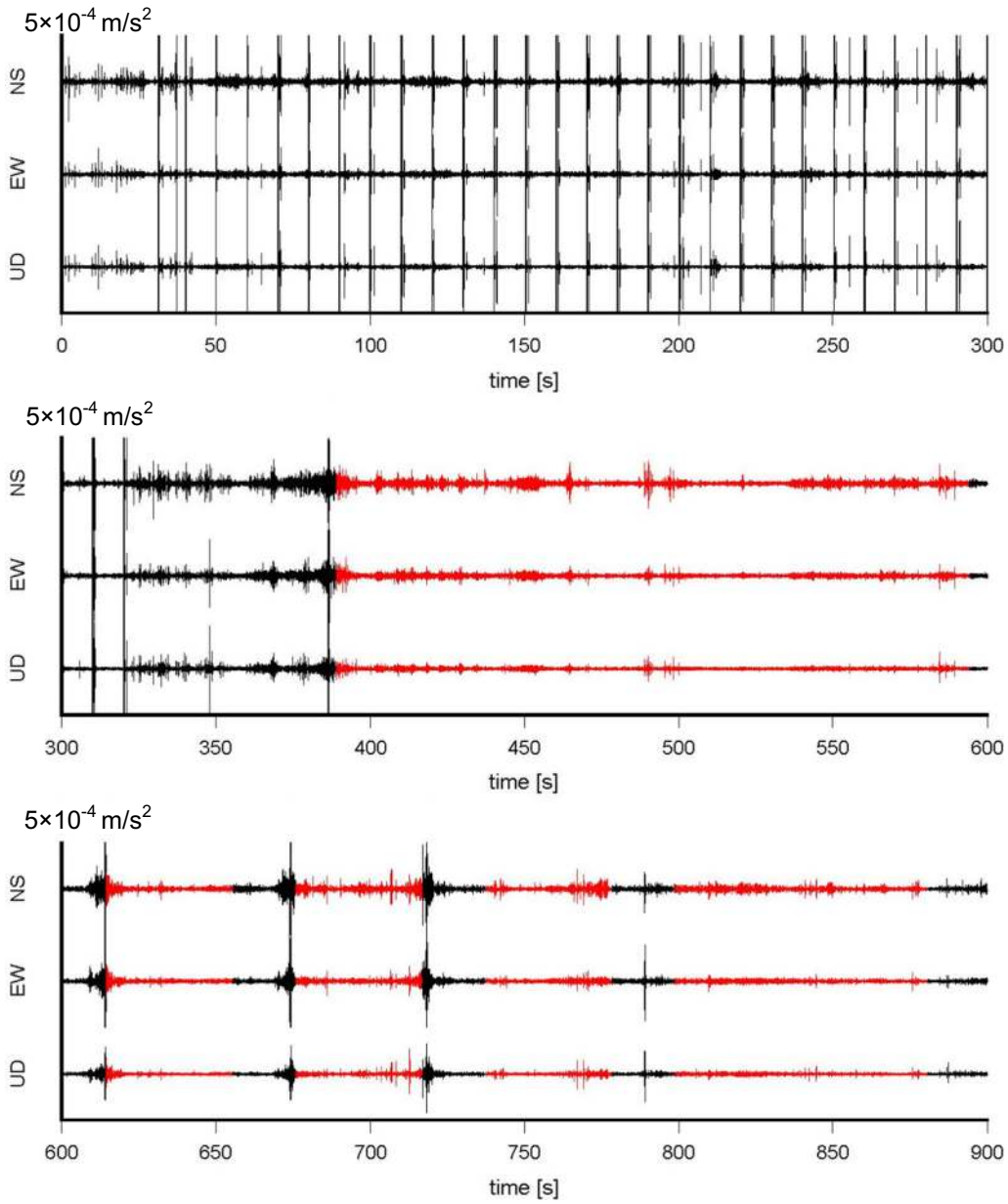

Fig. 4 Measured microtremor waveform at a measurement point EHM012. Red lines indicate parts used for analysis

$$\text{residual} = \sum \frac{\left(\log\left(\text{EHVR}_{\text{obs}}\right) - \log\left(\text{EHVR}_{\text{the}}\right)\right)^2}{f}. \tag{4}$$

Although for deep basin structures at K-NET and KiK-net sites we refer to the J-SHIS model in Japan, the S-wave velocity of the topmost layer in the J-SHIS database at a K-NET site is not always close to the S-wave velocity of the bottommost layer of the boring data since the depth of the K-NET boring is only 20 m at most. Thus, we need to introduce intermediate layers whose S-wave velocities are linearly increasing with depth with 200 m/s increment in between the bottommost layer of the boring data and the topmost layer of the J-SHIS database. In Table 2, we show an example of such an initial model creation process for EHM012.

We set the searching range of ± 30% for boring S-wave velocity data (while the layer thickness is fixed) and no range for J-SHIS thickness data (while the S-wave velocity is fixed). No range for thickness and velocity is assumed for the intermediate layers in between.

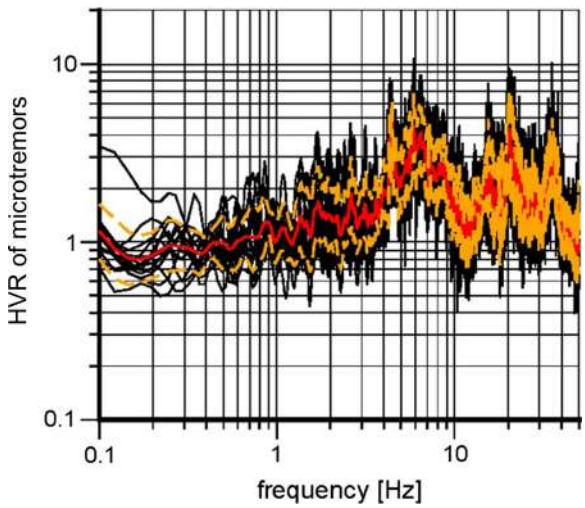

Fig. 5 MHVR at a measurement point EHM012. The averaged MHVR (red), the average ± one standard deviation (orange), and MHVRs for 15 segments (black)

In Fig. 6, we show matching of EHVRs at EHM012, a convergence path for 200 generations, and the shallow and deep S-wave velocity structures obtained, as an example. Blue lines in the last two panels are those for different trials with different initial sets of genes and green lines are for the initial model. We can see nice matching of the observed EHVR and very stable results in terms of obtained S-wave velocities for different trials.

Here we should emphasize the importance of the whole basin structure modeling down to the seismological bedrock in the EHVR inversion. As shown in the theoretical derivation of DFC, namely Eqs. 1–3, EHVR depends on the equipartitioned energy ratios at the seismological bedrock, α_H/β_H, and the transfer functions of P- and S-waves from there to the surface. This means that even in a high frequency range EHVR would be a function of the deep basin structure, not only a function of shallower sediments above the engineering bedrock.

To show the effects of a deep basin structure on EHVR in the high frequency range, we plot results of a parametric study in Fig. 7. We use the best-fit model with 14 layers as a reference for MYG004 (Nagashima et al. 2014, 2017) and omit two layers in each step from the bottom of the reference model. As the bottommost P- and S-wave velocities decrease, the peak in the lower frequency range disappears, as expected. However, not as expected, the peak and trough amplitudes in the higher frequency range increase strongly at the same time. This means that we should not invert only shallow sedimentary layers down to the engineering bedrock by using EHVR in the high frequency range as a target.

Results

EHVR and MHVR

Figure 8 shows comparisons of EHVRs and MHVR at six sites in Ehime Prefecture as an example. As pointed out before, EHVRs of the S-wave part and those of the coda part match with each other at most of the sites. The EHVR amplitude of the coda part tends to be a little smaller than that of the S-wave part, which is also pointed out in Satoh et al. (2001). This could be the effect of further energy scattering with time.

Comparison of EHVRs of the S-wave parts and MHVRs between 0.2 and 20.0 Hz shows that at most of the sites these two ratios are very close to each other, especially the amplitude and the frequency of the first peak, as seen in EHM08, EHM011, and EHM012 in Fig. 8. On the other hand, there are several sites where the HVR peak frequency is close, but the amplitude is different or both

Table 2 Shallow boring data, deep J-SHIS data, and the created initial model for EHM012

Shallow boring data

No.	Vs [m/s]	H [m]
1	290	5
2	590	5

Deep J-SHIS structure

No.	Vs [m/s]	H [m]
1	350	4
2	650	6
3	1200	10
4	1800	20
5	2400	60
6	3000	1915
7	3300	0

: Added layers

No.	Vs [m/s]	H [m]
1	290	5
2	590	5
3	790	1
4	990	1
5	1190	1
6	1200	7
7	1800	20
8	2400	60
9	3000	1915
10	3300	0

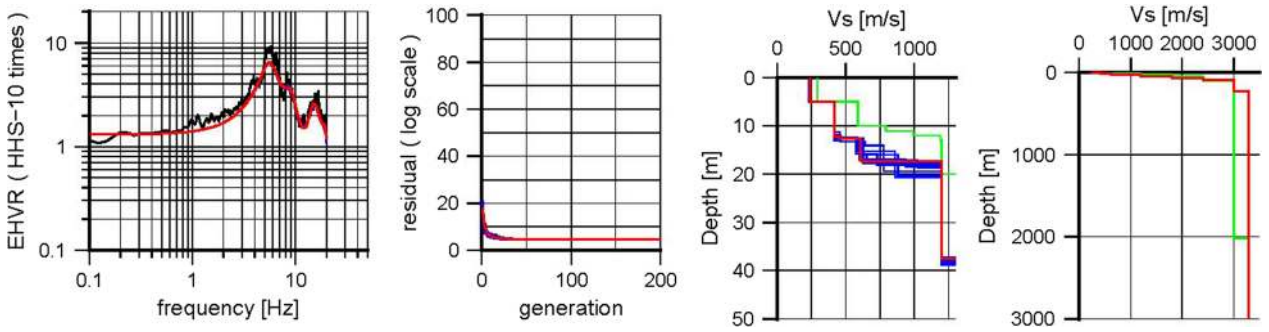

Fig. 6 Best-fit model (red line) in comparison with the observed EHVR (black line) in the left panel, convergence with respect to the generation in the middle panel, and shallow (< 50 m) and deep (< 3 km) part of the obtained S-wave velocities at a K-NET site, EHM012 in the two right panels. Green lines in the two right panels are S-wave velocities of the initial model, while blue lines are those for ten individual trials with different initial genes. The red line represents the best model among these ten trials

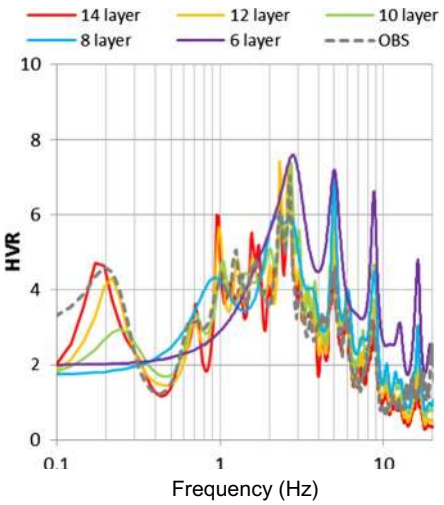

No.	Vs [m/s]	Vp [m/s]	H [m]	Depth [m]	Density [g/cm3]
1	42	709	2	2	1.54
2	64	756	2	4	1.57
3	116	865	3	7	1.63
4	128	891	5	12	1.64
5	257	1158	29	40	1.74
6	324	1296	34	74	1.78
7	464	1576	43	117	1.86
8	639	1916	502	619	1.94
9	872	2350	125	744	2.03
10	1133	2813	91	835	2.11
11	1593	3564	662	1497	2.25
12	2006	4171	238	1735	2.35
13	2404	4695	1245	2980	2.44
14	3400	5744	0	2980	2.64

Fig. 7 A parametric study of the effect of the bottommost layer on the theoretical EHVR for the best-fit model at MYG006 with 14 layers (Nagashima et al. 2014, 2017). When we omit the two layers in one step from the original velocity model shown in the right, not only the amplitude of the lowest frequency peak but also the amplitudes of peaks and troughs in the higher frequency range are strongly affected

are different, for instance EHM013 and EHM016. The notable difference is, however, that the EHVR amplitude after the first peak is much larger than that of the MHVR in general and sometimes it shows several clear peaks after the first one while the MHVR has smoothly varying characteristics in higher frequencies, as seen in EHM011. This kind of difference is exactly what we should expect due to the different nature of the wave field for microtremors and earthquakes.

Empirical EMR

The comparisons between EHVRs and MHVRs show that they are more or less similar until the fundamental peak frequency but that they are significantly different in the frequency range higher than that. Therefore, a way to extract a statistically significant trend in the difference between EHVRs and MHVRs is investigated. If we find a significant but common trend between EHVRs and MHVRs in all the sites, it means that we can convert MHVRs to equivalent EHVRs. To this end, we calculate the earthquake/microtremor ratio, EMR hereafter; the ratio of the average EHVR with respect to the average MHVR for each site as follows

$$\text{EMR} = \text{earthquke HVR/microtremor HVR.} \quad (5)$$

Figure 9 shows EMRs for individual sites and the EMR averaged over all the sites used, together with the average ± one standard deviation. We found that the EMR exceeds 1 from 1 to 30 Hz and that the maximum is around 10 Hz. This means that the amplitude of EHVR

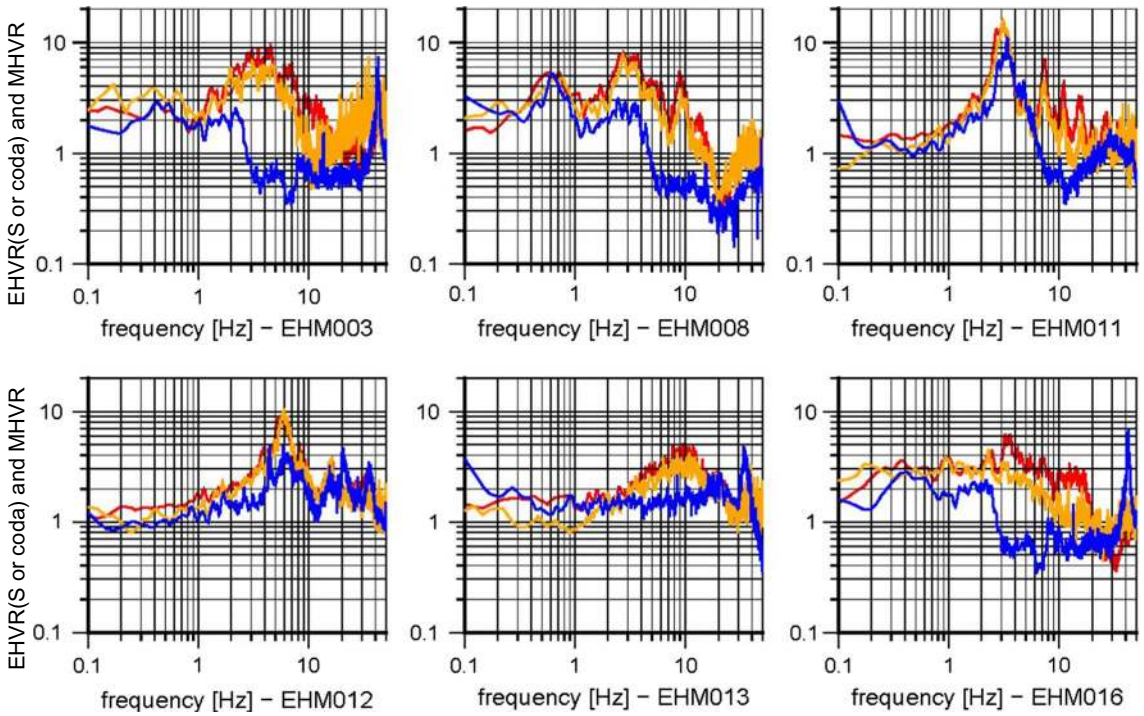

Fig. 8 Direct comparison of the average EHVRs of S-wave (red), the average EHVRs of S-coda (orange), and the average MHVRs for microtremors (blue) at six sites in Ehime Prefecture. MHVRs and EHVRs are quite similar for some sites, but MHVRs tend to be smaller for most of the sites

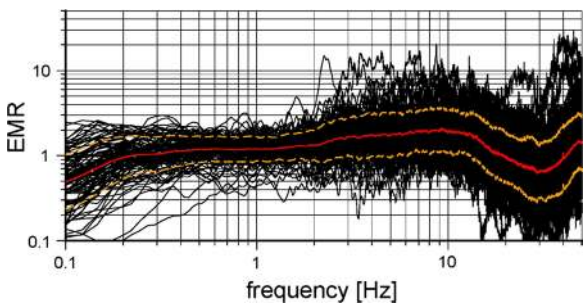

Fig. 9 Averaged EMR (red), the average ± one standard deviation (orange), and individual EMRs (black) for the 100 K-NET and KiK-net sites analyzed

is larger than MHVR for frequencies larger than 1 Hz, which is a direct consequence of the spectral difference shown in the previous section. However, these raw EMRs show large variations from site to site so that correction by using this simple averaged EMR may not be so meaningful.

When we look at the spectral comparison for individual sites in Fig. 8 and other sites omitted here, we can see clear frequency characteristics in the difference between EHVR and MHVR as mentioned before. Assuming that the fundamental peak frequencies of EHVR and MHVR are basically the same, which should reflect the specific velocity structure at that site, we can expect similar spectral characteristics in the EMRs for sites with similar fundamental peak frequencies. This is because EMRs are a direct consequence of the wave field difference of earthquake and microtremor ground motions in the same velocity structure. Therefore, the average EMR for a normalized frequency is derived by reading the fundamental peak frequency of MHVR and normalizing the frequency of EMR with respect to this fundamental peak frequency. To suppress some spurious peaks, we use a 0.3-Hz Parzen window on MHVR when we read the fundamental peak frequency. Here, from a practical view point, we would like to restrict EMR calculations for the sites with a clear peak in between 0.2 and 20.0 Hz, so sites with MHVRs whose first peak is less than 2 in amplitude or whose first peak frequency is below 0.2 Hz or over 20.0 Hz are excluded from further analysis. As a result, 87 sites are selected for the averaging operation to get the normalized EMR. Figure 10 shows the average EMR with respect to the normalized frequency, together with the numbers of data used for averaging at each normalized frequency. If the fundamental peak frequency is high, then normalized frequency will become small and so such a site will contribute large numbers of data in the lower frequency range as we can see in the lower panel of Fig. 10. The

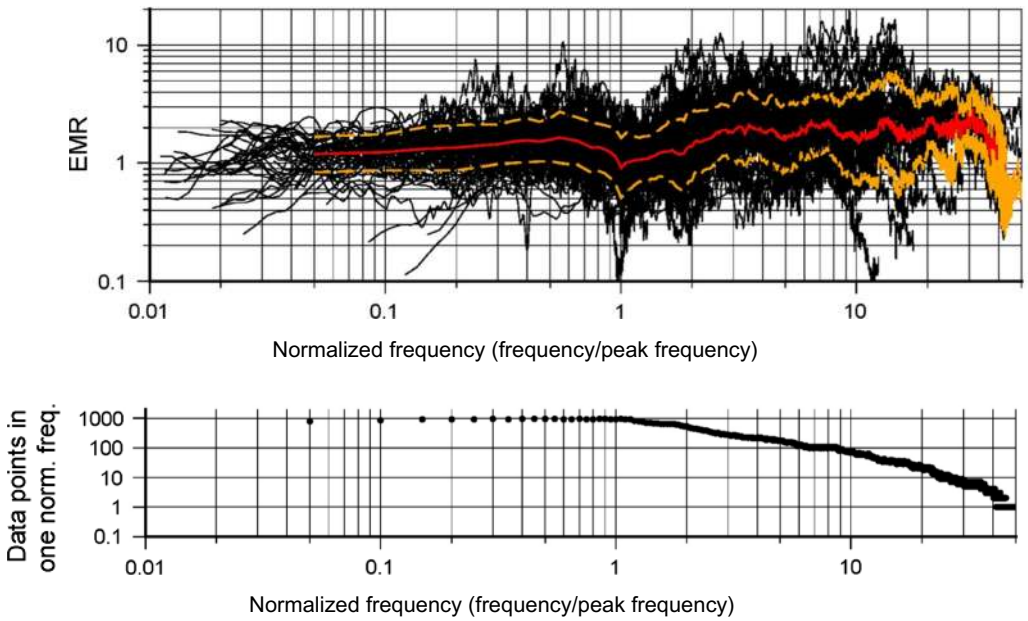

Fig. 10 Averaged EMR (red), the average ± one standard deviation (orange), and individual EMRs (black) where the horizontal axis at all the sites are normalized with respect to their fundamental peak frequencies of MHVRs. The lower panel shows the numbers of data used for averaging at each normalized frequency (with respect to the peak frequency) with the equal increment of 0.05. Since many frequency points will be provided from the sites with high fundamental peak frequencies, numbers below 1 are much larger

interval along the horizontal axis differs for each sites because of normalization. To calculate the average EMR shown by the red line, the common interval $\Delta = 0.05$ is designated and the log-average is taken for all the data that fall into the frequency band ± 0.025 around the target frequency.

The frequency range of averaged EMRs extends into very low frequencies because of the data with higher (> 10 Hz) fundamental peak frequencies, and the average EMR is dropped to 0.3 at the highest frequency end because the number of data used is too small. The precision at both ends of the EMR is considered to be low as the interval between normalized frequencies would be too large when the peak frequency is below 1.0 Hz and the interval would be too small when the peak frequency is above 10 Hz. This means that the density of the frequency sampling from site to site can be considerably different because of the difference of the fundamental peak frequency. Also it would be more physically meaningful to have different correction factors depending on the fundamental peak frequencies. Therefore, these EMRs are categorized based on the fundamental peak frequency and the average EMR is calculated in each category. Figure 11 shows the average frequency-normalized EMRs in five peak frequency categories, namely 0.2–1, 1–2, 2–5, 5–10 and 10–20 Hz, together with their deviation ranges. We may get a smaller variation if we use a smaller frequency range but then the reliability of the average EMR will be decreased since the number of the sites in one category will be decreased. Table 3 shows the peak frequency range, number of measurement points, and interval Δ used in averaging in each category.

In Fig. 11, distinctive features are evident in different categories. Most notably, the EMR after the fundamental peak (i.e., $f\_\text{normal} \geqq 2.0$) is especially large when the fundamental peak frequency is between 0.2 and 5.0 Hz (i.e., Category 1–3). Figure 12 shows the average EMRs of all the five categories, together with the whole average EMR without categorization (shown in Fig. 10). The average EMR in each category shows a similar amplitude in the frequency range with overlapping, but they are not exactly the same, especially when the normalized frequency is between 2 and 10. This means that average EMRs calculated in each category here should be used for better representation of EMRs, not the EMR without category classification.

We should note that the trend below 1 is somewhat different from category to category because we may have a secondary peak or peaks below 1 if we choose the fundamental peak frequency in the high frequency range (as Category 4 and 5), while we may hardly have a secondary peak or peaks below 1 if we choose the fundamental peak

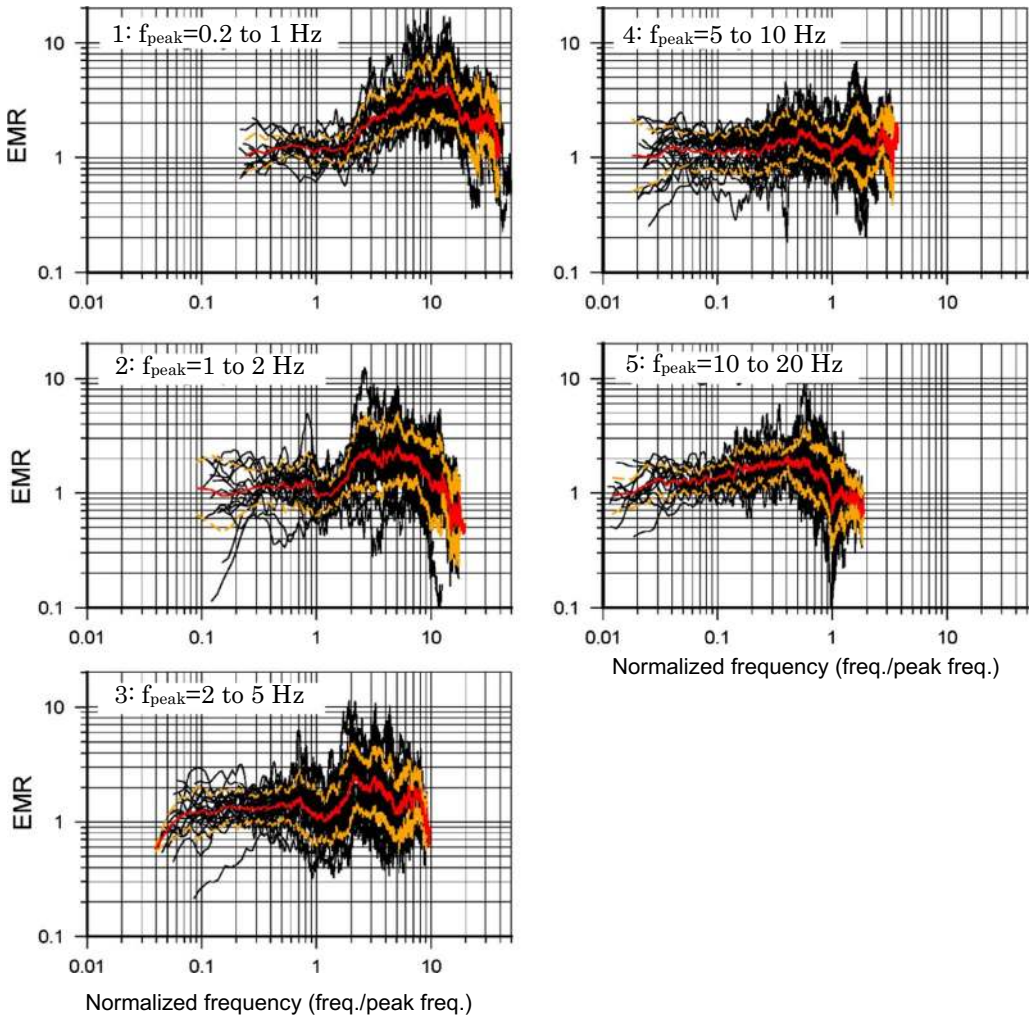

Fig. 11 Average EMRs with normalized frequency categorized by peak frequency ranges. Peak frequency range is: top left: 0.22–1.0 Hz, middle left: 1.02–2.0 Hz, bottom left: 2.0–5.0 Hz, top right: 5.02–10.0 Hz, and middle right: 10.02–20.0 Hz. Red lines are the log-averaged values, which are used for pEHVR calculation, while orange lines are the average ± one standard deviation. The horizontal axis is the normalized frequency for each category. We can see that significant correction factors are needed in the normalized frequency range higher than 2 for Categories 1–3

Table 3 Detailed statistics of five categories

	Category 1	Category 2	Category 3	Category 4	Category 5
Peak freq. (Hz)	0.2–1.0	1.0–2.0	2.0–5.0	5.0–10.0	10.0–20.0
Numbers	15	17	21	20	14
Δ	0.06	0.03	0.013	0.006	0.003

frequency in the lower frequency range (as Category 1 and 2). For Category 4 and 5, a high frequency peak has the highest amplitude but we may also have smaller peaks in the lower frequency range where we would have difference in EMR with smaller degree as shown in Fig. 12.

Validity of pEHVR

Once we obtain the average empirical EMR, we can translate MHVRs into pseudo-EHVRs, or simply pEHVR. To see the validity of the EMR correction, we plot comparisons of EHVR, MHVR, and pEHVR in Fig. 13 for three representative sites in Category 1 (0.2–1 Hz peak) and Fig. 14 for three sites in Category 3 (2–5 Hz peak). As we can see in these figures, correction by EMR to MHVR is quite effective for reproducing EHVRs for most of the sites. When we compare correlations between MHVR and EHVR and between pEHVR and EHVR, significant improvement in the latter can be seen, especially for sites with high peak amplitude. Thus, EMR correction is meaningful to make MHVR closer to EHVR.

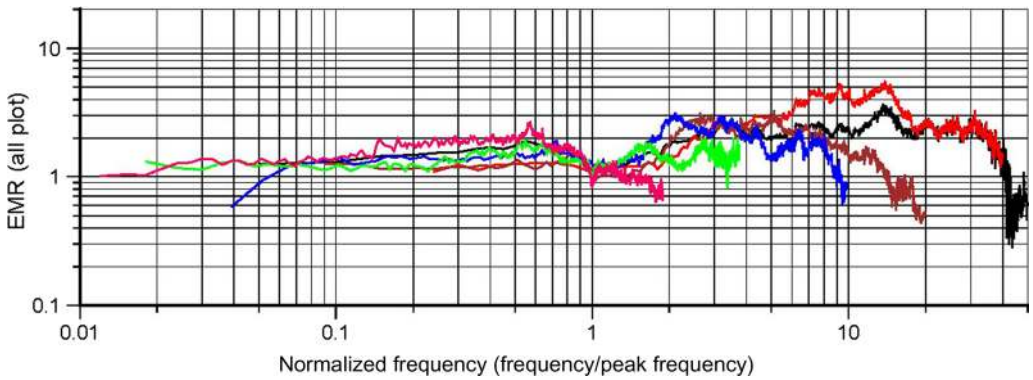

Fig. 12 Comparison of the average EMRs for five categories with the EMR for the whole frequency without categorization (Fig. 10). Peak frequency exists in (red) 0.1–1.0 Hz, (brown) 1.02–2.0 Hz, (blue) 2.02–5.0 Hz, (green) 5.02–10.0 Hz, (pink) 10.02–20.0 Hz, and (black) all EMRs

Inversions for MHVR and pEHVR

The effectiveness of EMR correction should be measured whether we can invert a similar velocity structure or not by using pEHVR as a substitute. In Fig. 15, we plot the same figures as in Fig. 6, but the results are plotted using pEHVR at EHM012. We can see that a similar velocity structure is inverted from pEHVR.

We should note that, if we directly substitute MHVR for EHVR and perform inversion analysis based on the theory of EHVR (i.e., Eq. 3), we can still find a very nice matching to data (i.e., MHVR). However, the resultant velocity structure is not exactly the same as the one obtained from the observed EHVR. This is because MHVR tends to be smaller than EHVR in the frequency range higher than the fundamental peak frequency as mentioned already, which makes impedance contrasts within layers smaller. Such an example is shown in Fig. 16 again for EHM012. The inverted structure by using MHVR has a high velocity layer between 5 and 20 m since the peak amplitude of MHVR is smaller than that of EHVR.

Finally, we performed the same inversion analyses using EHVRs, pEHVRs, and MHVRs for 87 sites in which the fundamental peak frequency falls into 0.2–20 Hz. To show the effectiveness of pEHVR for velocity inversion in comparison with the direct use of MHVR for all the sites, we plot averaged S-wave velocities down to the depth z, Vs_z, of inverted structures using Eq. 6, where z is chosen to be 10, 30, and 100 m.

$$\mathrm{Vs\_}z = \frac{z}{\sum_{i=1}^{N} \frac{H_i}{\mathrm{Vs}_i}} \tag{6}$$

Here, H_i is the thickness of the ith layer, Vs_i is the S-wave velocity of the ith layer, and N is the number of layers down to the depth z.

Figure 17 shows the comparison of obtained Vs_10, Vs_30, and Vs_100 from MHVRs (left) and pEHVRs (right) in the vertical axes with respect to those from the true EHVRs in the horizontal axis. Here the identified results for EHVR are considered to be the correct solution. It is apparent that pEHVRs can reproduce very similar Vs_10 and Vs_30 and keep a 1–1 correspondence on the average. On the other hand, if we use MHVRs directly, the resultant Vs_10, Vs_30, and Vs_100 have a larger deviation and systematic bias at higher-velocity (stiff) sites. This figure provides supporting evidence to promote our method in which we use empirical EMRs to translate MHVRs into pEHVRs.

Discussion

Validation in Sendai: data

So far, the operation is circular except for taking the average of EMRs for different categories based on fundamental peak frequencies of MHVRs. We need independent evidence to support the validity of the empirical EMR operation for better inversion of velocity structures.

To that end, we used seven sites in Sendai, Miyagi Prefecture, where prior underground structure information as well as earthquakes and microtremors data exist. Sendai City suffered from the 1978 Miyagi-ken Oki earthquake of M7.4 as well as the 2011 Off the Pacific Coast of Tohoku earthquake of M9.0. The city is located close to the active Nagamachi-Rifu fault. Satoh et al. (2001a, b) carried out array microtremor measurements in Sendai and nearby cities to obtain the deep S-wave velocity structures inside the Sendai basin, and the earthquake ground motions were also measured at the center of each array. The array measurement locations at Sendai are shown in Fig. 18. Among these sites, the same analysis

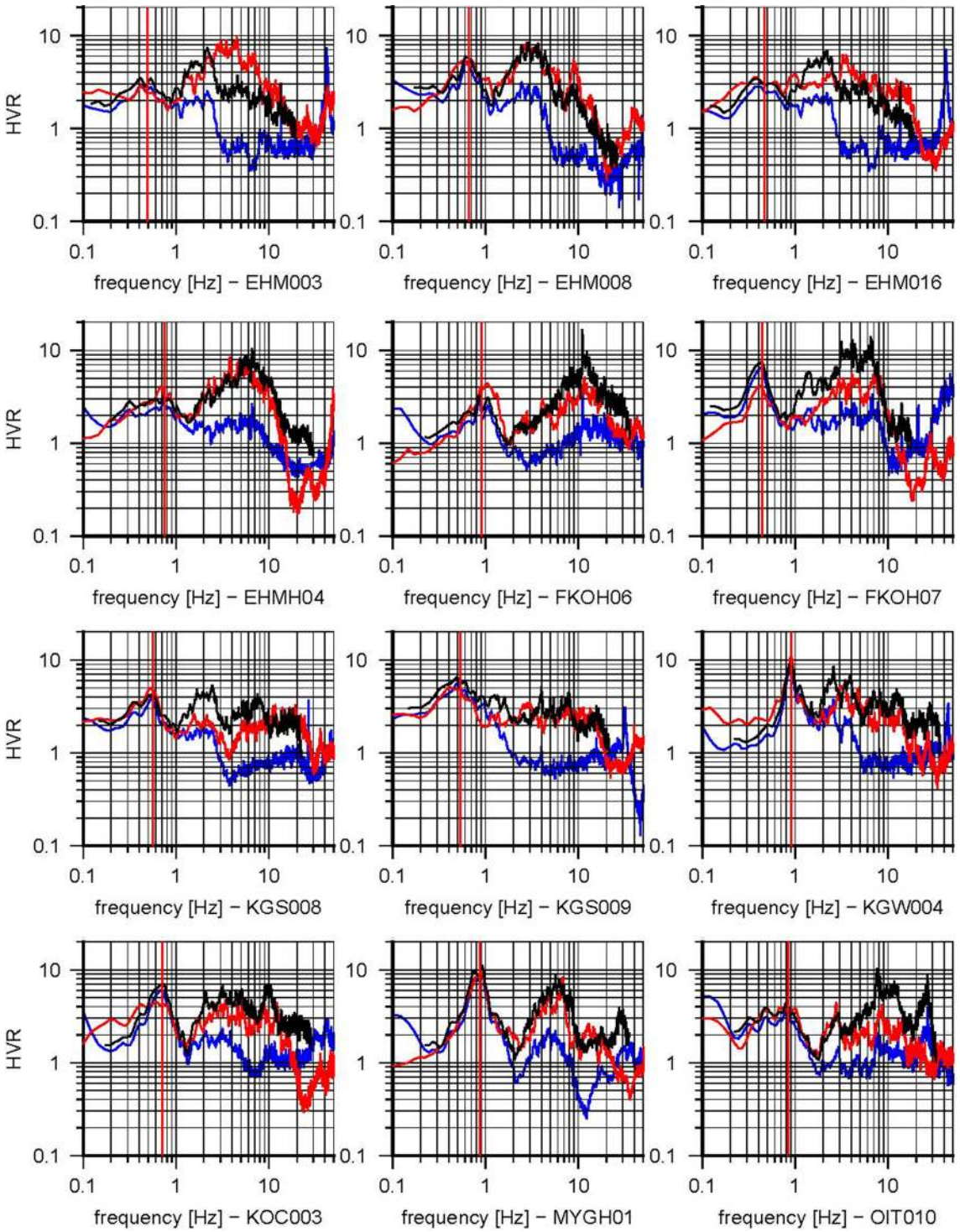

Fig. 13 Direct comparison of the EHVRs of S-wave (red), the MHVRs for microtremors (blue), and the pEHVRs translated from MHVR by using the empirical EMR of Category 1 (black). We can see significant shift of amplitude toward EHVR. Red vertical lines are the fundamental peak frequencies used

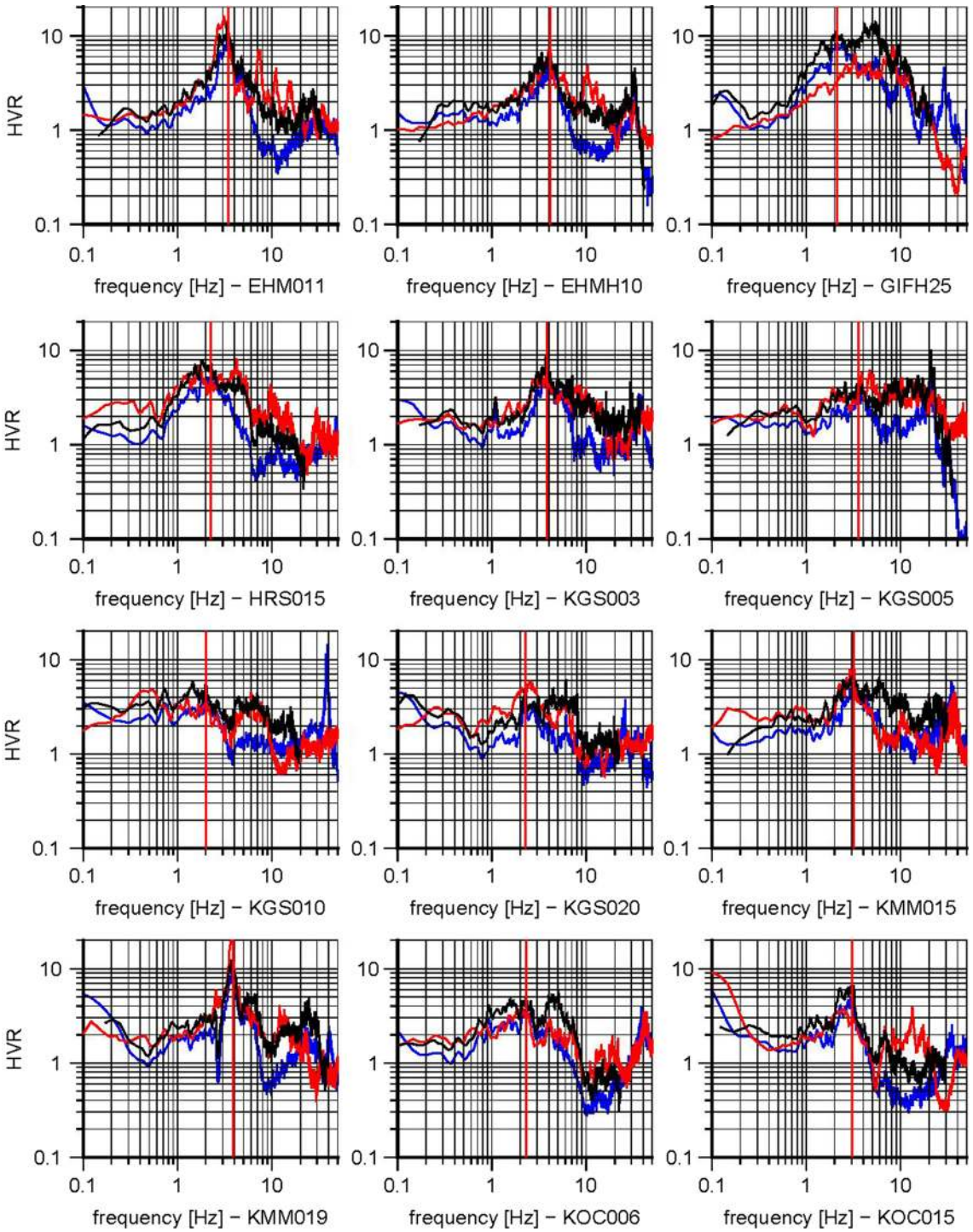

Fig. 14 Same comparison as Fig. 13 but for sites with Category 3

for validation is conducted using earthquake and microtremor HVRs at seven sites, namely ARAH, MYG015, NAGA, NAKA, SHIR, TRMA, and TAMA. Although velocity structures at these sites are different from each other, the characteristics of the wave field either for earthquake or microtremors are considered to be basically one-dimensional because of the isotropic nature of their HVRs.

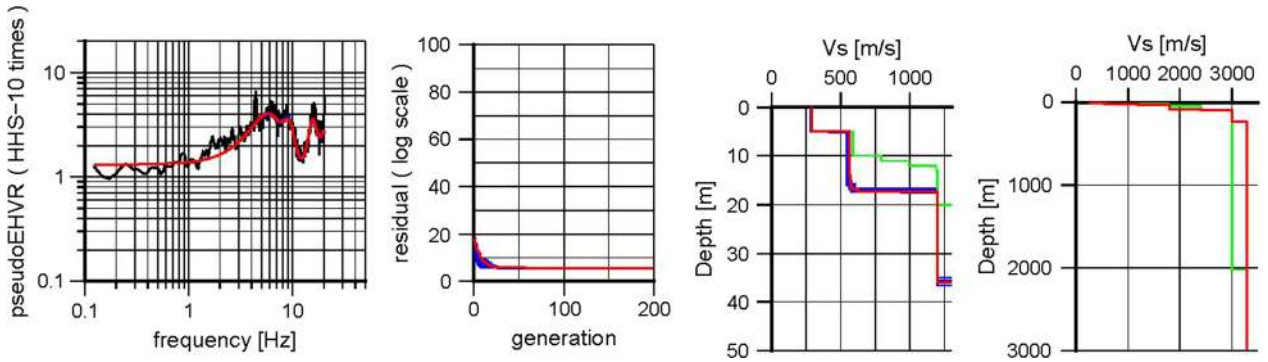

Fig. 15 Best-fit model (red line) in comparison with the translated pEHVR (black line) in the left panel, convergence with respect to the generation in the middle panel, and shallow (< 50 m) and deep (< 3 km) parts of the obtained S-wave velocities at EHM012 in the two right panels. Blue lines are those for ten trials with different genes, while red lines are values of the best model. Green lines in the two right panels are S-wave velocities of the initial model

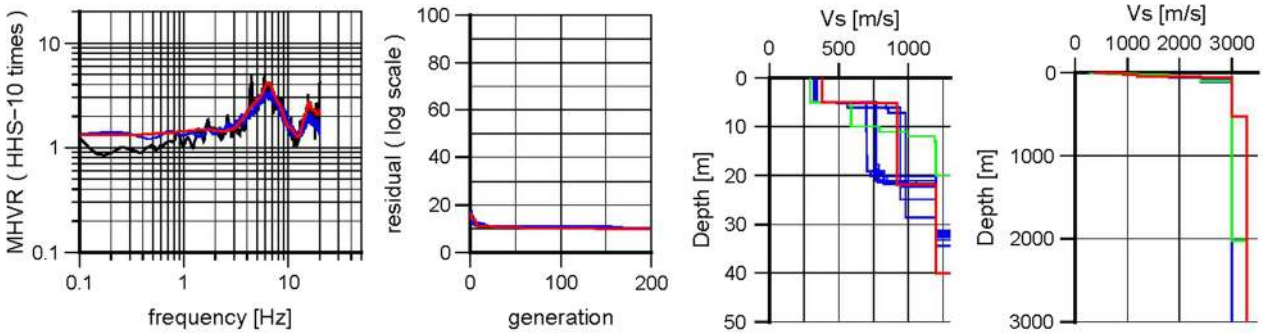

Fig. 16 Best-fit model (red line) in comparison with the observed MHVR (black line) in the left panel, convergence with respect to the generation in the middle panel, and shallow (< 50 m) and deep (< 3 km) parts of the obtained S-wave velocities at EHM012 in the two right panels. Blue lines are those for ten trials with different genes, while red lines are values of the best model. Green lines in the two right panels are S-wave velocities of the initial model. We should note that here we used the formula for earthquake (i.e., Eq. 3), not for microtremors

Figure 19 shows the pEHVRs derived from MHVRs and EMRs, EHVR, and MHVRs at seven sites in Sendai. Compared to the observed ones, clear fundamental peaks exist in the low frequency range of 0.2–1.0 Hz in both MHVR and EHVR and the peak levels roughly agree at all the sites except for TAMA. However, upon closer inspection, the peak amplitudes of EHVRs are slightly smaller at NAGA and SHIR but that of EHVR is larger at TRMA. Furthermore, the amplitude levels of MHVR are much smaller than EHVRs at 1.0 Hz and above in all the sites. There is a peak near 3.0 Hz in EHVR at TAMA, but its amplitude is rather small and there is no corresponding peak in MHVR.

Next, pEHVR, which is calculated using MHVR and EMR that corresponds to a proper category for the fundamental peak frequency, and EHVR are compared. At ARAH, NAGA, NAKA, and MYG015, pEHVR and EHVR agree very well. The peak amplitude at about 3 Hz of pEHVR at SHIR exceeds that of EHVR since the peak amplitude of MHVR is already large, although in the frequency range from 1 to 3 Hz EMR correction did a reasonably good job. On the other hand, pEHVR at TRMA could not provide the correct second peak frequency at around 4 Hz, although the overall amplitude in the high frequency range becomes closer to the EHVR than that of MHVR is. Since no clear peaks are found in MHVR at TAMA, the site is excluded from underground structure identification.

Validation in Sendai: with a priori constraints

The underground structure models identified by Satoh et al. (2001a) are set as the initial models with a priori information, and the underground structure is inverted using the inversion method described above. Table 4 shows the initial models with a priori information. The bottom three layers are set to Vs = 850, 1700, and 3500 m/s in all the cases. The velocity structure of layers above the Vs = 850 m/s layer and the numbers of layers differ from site to site.

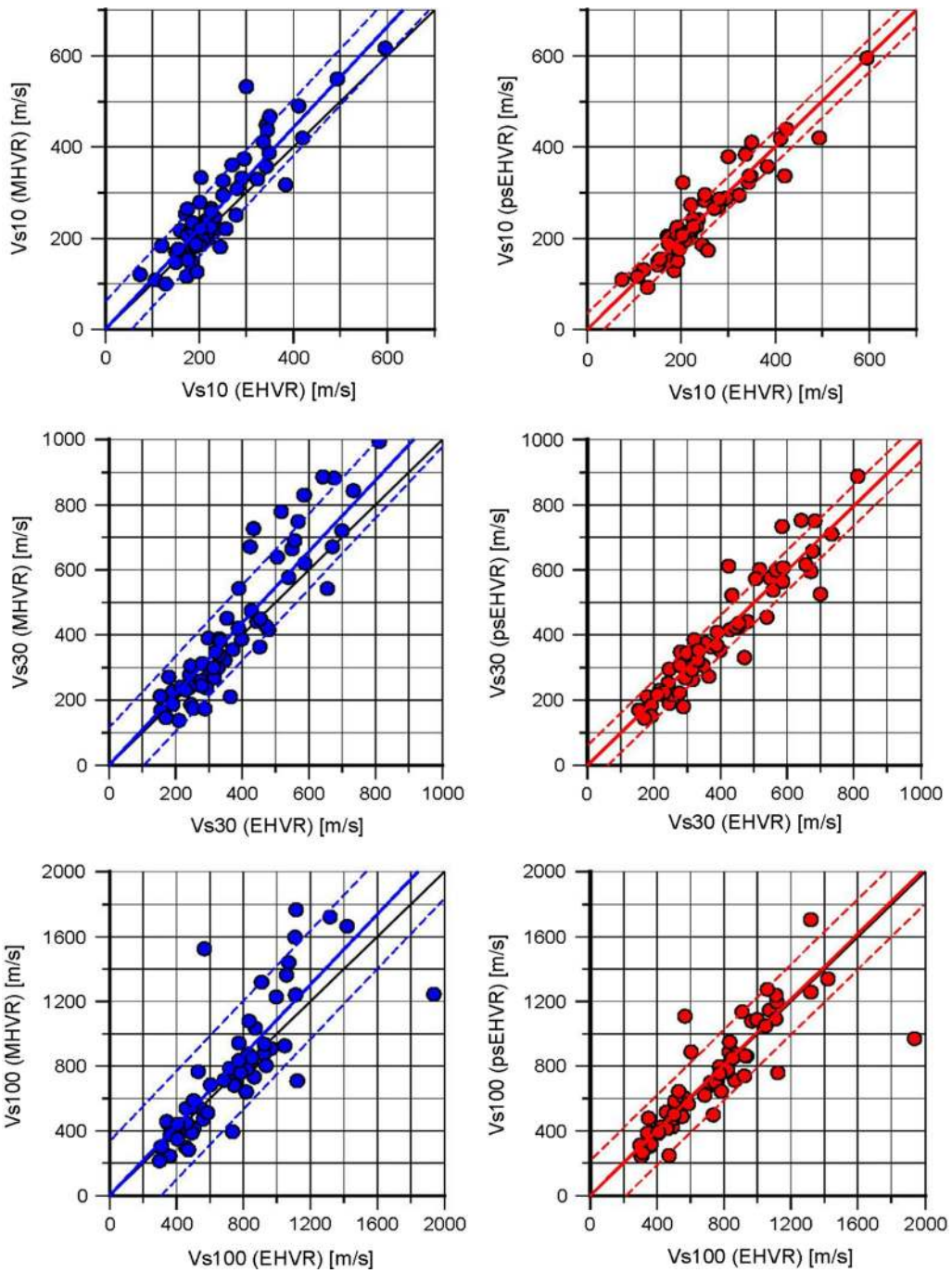

Fig. 17 Comparison of the averaged velocities from pEHVR inversion or MHVR inversion (vertical axis) with respect to those from EHVR inversion (horizontal axis). Each panel shows those for top 10 m (top), 30 m (middle), and 100 m (bottom). Inversions from MHVR (left) and those from pEHVR (right)

The same inversion scheme is carried out using EHVR, pEHVR, and MHVR as the target. The only difference is that the searching range in the inversion is limited to $\pm$ 30% of the initial model for all the layers because the initial values from Satoh et al. (2001a) would be more or less reliable.

First focusing on inversion results using EHVR as the target, the measured EHVR agrees better with the inverted result of EHVR than the initial model of EHVR for most of the sites, which is a natural consequence. The only exception is the amplitude at high frequency above

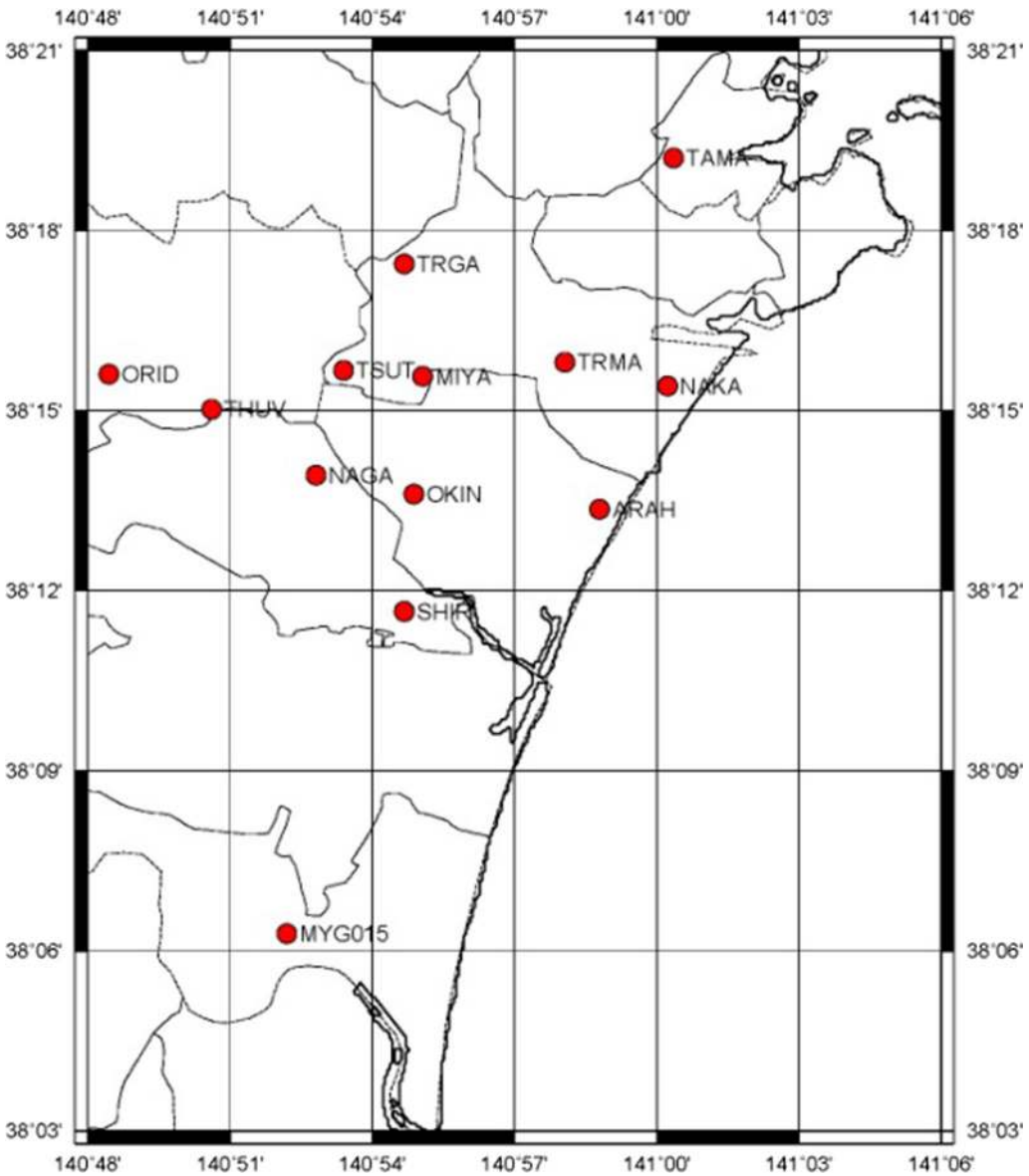

Fig. 18 Microtremor and earthquake ground motion measurement sites in and around Sendai City

4.0 Hz at NAGA, where the inverted model cannot sufficiently reach the observed high amplitude. In Figs. 20 and 21, we show matching HVRs, convergence paths of residuals, and the final inverted velocity models for EHVR, pEHVR, and MHVR cases for MYG015 and TRMA.

Looking at the inversion results using pEHVR and MHVR at each site, the identified velocity structures from both pEHVR and MHVR are found to successfully reproduce the target HVRs. However, the resultant velocity structure from MHVR is not similar to that from EHVR, while that from pEHVR is much closer to that from EHVR, as can be seen in Figs. 20 and 21. At TRMA in Fig. 21, high-frequency amplitude in MHVR is much smaller than the EHVR so that the inverted shallow velocity structure from MHVR yields a strong velocity inversion (a high-speed layer in a shallower depth) at 20 m, which is softened in either the velocity structure from EHVR or that from pEHVR. Although figures are omitted, again inversion from pEHVR cannot explain the amplitude above 4.0 Hz at NAGA, as in the case of EHVR. Interestingly, however, inversion from MHVR can reproduce the amplitude above 4.0 Hz at NAGA, since the amplitude of MHVR does not show any prominent peaks in that high frequency range.

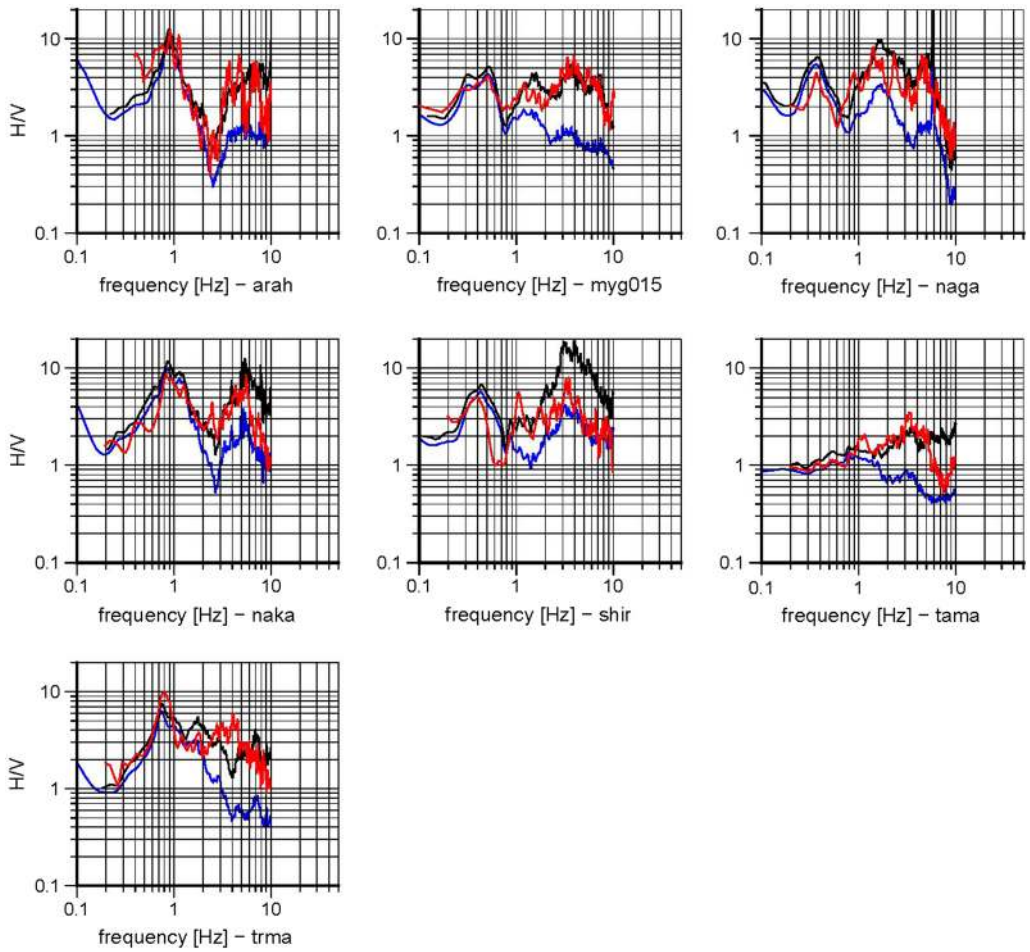

Fig. 19 Comparison of EHVRs (red), MHVR (blue), and pEHVR (black) at seven sites in Sendai

Validation in Sendai: without a priori constraints

Underground structure inversion without a priori constraint, such as PS logging data from boring, could be ideal when actually inverting the underground structure using pEHVR alone. To test the initial model dependence, the J-SHIS underground structure model publicly available from NIED is used as the initial value. Table 5 shows the initial model based on J-SHIS. There are only two layers with an S-wave velocity (Vs) less than 1200 m/s in the J-SHIS underground structure, which have Vs = 350 and 650 m/s, and so one layer with the initial S-wave velocity Vs = 200 m/s is added to the surface of the model.

As in the previous section, EHVR, pEHVR, and MHVR are set as the target and ten independent HHS inversions are conducted for each target. The S-wave velocity and layer thicknesses are considered as variables in all layers without setting any range of variation because the initial model information is not considered to be so reliable. However, the minimum S-wave velocity at the surface layer is set to be Vs = 50 m/s for reality. Figures 22 and 23 show a comparison of inverted results at MYG015 and TRMA. We found that the matching for EHVR, pEHVR, and MHVR with the resultant inverted structures is in general as good as the case with the initial models. This means that initial model dependency is not so strong as long as we give sufficient space for variables. It is especially interesting to see the better matching of the inverted EHVR and pEHVR at NAGA; now both structures can reproduce a high amplitude peak at 4.0 Hz. The resultant residuals without a priori information are much smaller than those with a priori information.

Again looking at the velocity models from MHVRs, we found that they are different from the velocity models from EHVRs and pEHVRs, although their convergences are sometimes better than those of EHVRs and pEHVRs. This discrepancy suggests that it is not appropriate to directly substitute MHVRs in the inversion based on the diffuse field concept for earthquake ground motions.

Table 4 Initial underground structures based on the previous study at each site (Satoh et al. 2001)

No.	Thickness (m)	Depth (m)	Vp (m/s)	Vs (m/s)	Density (g/cm^3)	No.	Thickness (m)	Depth (m)	Vp (m/s)	Vs (m/s)	Density (g/cm^3)
ARAH						*NAKA*					
1	2.0	2.0	290.0	122.8	1.70	1	2.2	2.2	320.0	70.7	1.70
2	4.0	6.0	1570.0	161.0	1.80	2	3.4	5.6	970.0	163.8	1.70
3	8.0	16.0	1570.0	261.4	1.80	3	3.1	8.7	970.0	209.7	1.90
4	6.9	22.9	1570.0	192.1	1.75	4	6.8	15.5	1550.0	209.7	1.90
5	4.9	27.8	1150.0	192.1	1.75	5	8.3	23.8	1550.0	172.9	1.80
6	5.3	33.1	1150.0	105.5	1.75	6	5.2	29.0	1650.0	220.0	1.80
7	3.9	37.0	1660.0	397.4	1.95	7	8.8	37.8	1650.0	337.4	1.90
8	14.7	51.7	1660.0	570.0	1.90	8	8.7	46.5	1650.0	319.5	1.80
9	25.9	77.6	1880.0	610.0	1.85	9	14.6	61.1	2150.0	487.3	1.95
10	180.2	257.8	2000.0	850.0	2.10	10	100.0	161.1	2000.0	850.0	2.10
11	294.4	552.2	3300.0	1700.0	2.34	11	200.0	361.1	3300.0	1700.0	2.34
12	∞	∞	6100.0	3500.0	2.70	12	∞	∞	6100.0	3500.0	2.70
SHIR						*TRMA*					
1	2.8	2.8	180.0	101.1	1.65	1	1.3	1.3	290.0	87.4	1.60
2	7.2	10.0	1310.0	171.7	1.70	2	0.7	2.0	290.0	87.4	1.75
3	3.3	13.3	1310.0	274.0	1.80	3	2.3	4.3	690.0	87.4	1.75
4	2.7	16.0	1970.0	274.0	1.85	4	12.0	16.3	1630.0	184.1	1.75
5	4.0	20.0	1970.0	464.1	2.00	5	3.0	19.3	1630.0	243.6	1.70
6	18.0	38.0	1970.0	538.8	2.00	6	5.2	24.5	1630.0	186.4	1.70
7	22.5	60.5	1830.0	477.1	2.00	7	21.5	46.0	1870.0	398.1	1.90
8	3.0	63.5	2000.0	612.1	2.10	8	12.8	58.8	1870.0	604.4	2.00
9	9.1	72.6	2000.0	612.1	2.15	9	2.7	61.5	1870.0	363.3	1.90
10	3.4	76.0	2000.0	612.1	2.10	10	4.4	65.9	1870.0	563.8	2.00
11	351.0	427.0	2000.0	850.0	2.10	11	5.4	71.3	1870.0	384.2	1.85
12	677.0	1104.0	3300.0	1700.0	2.34	12	7.7	79.0	1870.0	416.0	1.90
13	∞	∞	6100.0	3500.0	2.70	13	158.1	237.1	2000.0	850.0	2.10
						14	300.0	537.1	3300.0	1700.0	2.34
						15	∞	∞	6100.0	3500.0	2.70

Table 4 continued

No.	Thickness (m)	Depth (m)	Vp (m/s)	Vs (m/s)	Density (g/cm^3)	No.	Thickness (m)	Depth (m)	Vp (m/s)	Vs (m/s)	Density (g/cm^3)
MYG015						*NAGA*					
1	2.0	2.0	370.0	100.0	1.56	1	8.0	8.0	240.0	81.9	1.65
2	2.0	4.0	1600.0	100.0	1.62	2	4.1	12.1	920.0	81.9	1.65
3	4.0	8.0	1600.0	180.0	1.74	3	4.4	16.5	1600.0	271.6	1.95
4	9.0	17.0	1600.0	250.0	1.85	4	11.0	27.5	1050.0	154.2	1.70
5	79.1	96.1	1600.0	410.0	1.97	5	8.2	35.7	1640.0	287.0	1.75
6	266.0	362.1	2000.0	850.0	2.10	6	28.0	63.7	1990.0	581.1	2.10
7	565.9	927.0	3300.0	1700.0	2.34	7	24.5	88.2	1700.0	515.5	1.95
8	∞	∞	6100.0	3500.0	2.70	8	370.0	458.2	2000.0	850.0	2.10
						9	740.0	1198.2	3300.0	1700.0	2.34
						10	∞	∞	6100.0	3500.0	2.70

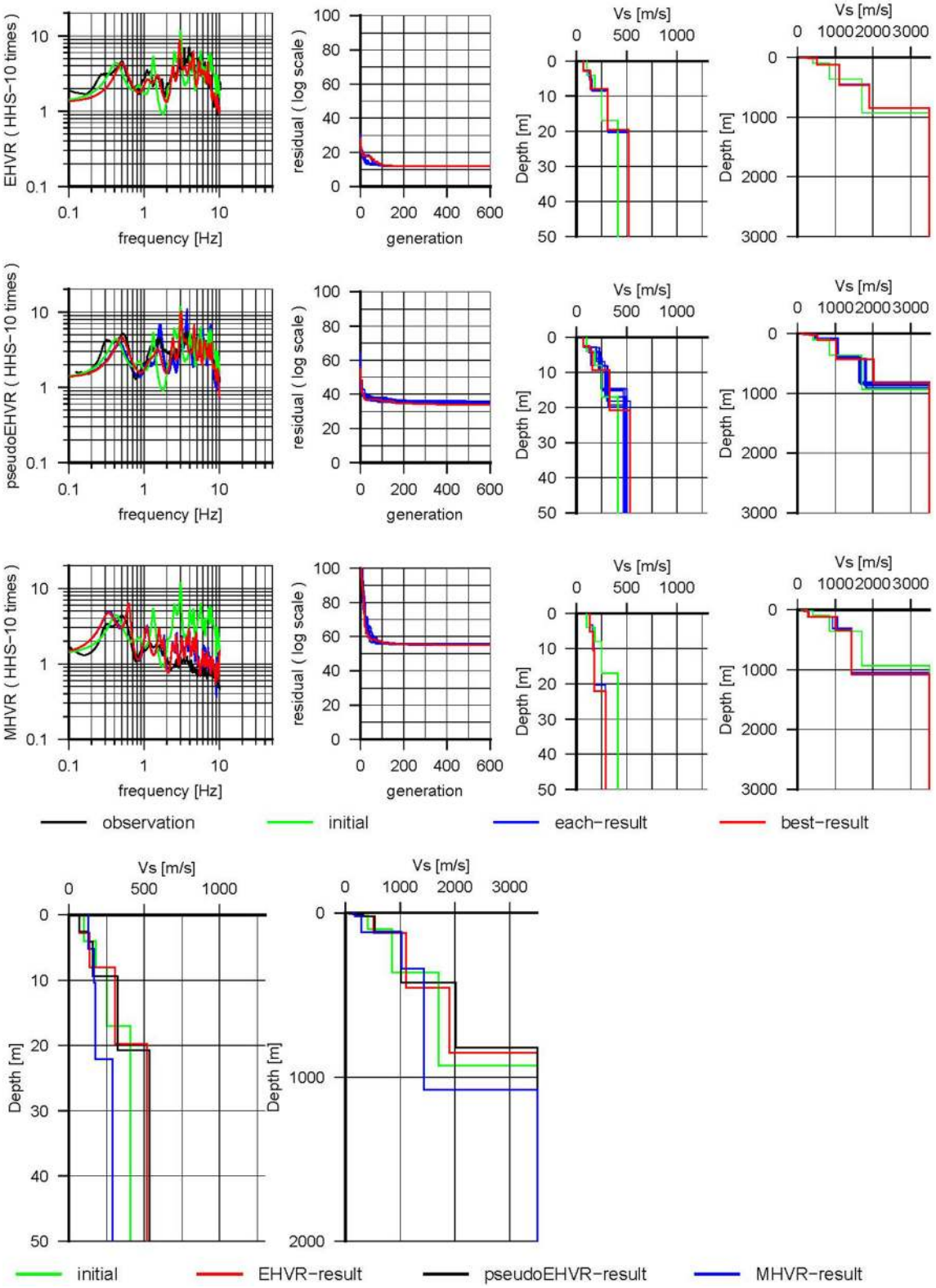

Fig. 20 Inversion results at MYG015 when a priori underground structure model of Satoh et al. (2001a) is used as the initial model. The target is (top row) EHVR, (second row) pEHVR, and (third row) MHVR. The left column shows comparison of HVRs, and the second left column shows process of residual convergence with respect to the generation. Two right columns show resultant shallow and deep velocity structures. The bottommost row shows comparison of inverted underground structures from three targets

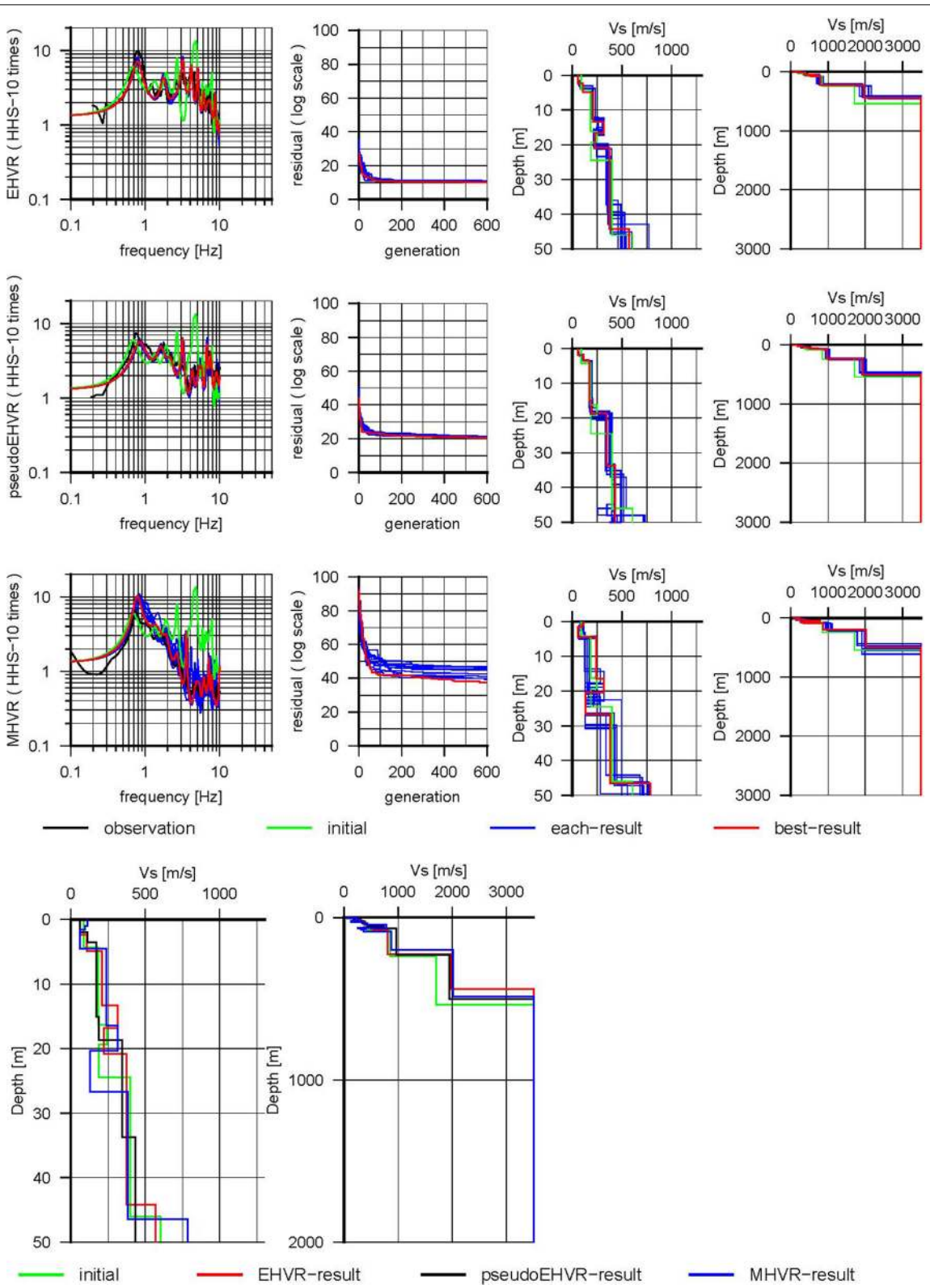

Fig. 21 Inversion results at TRMA when a priori underground structure model of Satoh et al. (2001a) is used as the initial model

Table 5 Initial underground structure based on the J-SHIS data

No.	Thickness (m)	Depth (m)	Vp (m/s)	Vs (m/s)	Density (g/cm^3)	No.	Thickness (m)	Depth (m)	Vp (m/s)	Vs (m/s)	Density (g/cm^3)
ARAH						*NAGA*					
1	22.0	22.0	1000.0	200.0	1.85	1	40.0	40.0	1200.0	200.0	1.75
2	44.0	44.0	1600.0	350.0	1.85	2	40.0	80.0	1600.0	350.0	1.85
3	97.0	141.0	2000.0	650.0	1.95	3	97.0	177.0	2000.0	650.0	1.95
4	10.0	151.0	2300.0	900.0	1.95	4	10.0	187.0	2300.0	900.0	2.05
5	25.0	176.0	2600.0	1200.0	2.15	5	272.0	459.0	2600.0	1200.0	2.15
6	58.0	234.0	3200.0	1500.0	2.25	6	161.0	620.0	3200.0	1500.0	2.25
7	101.0	335.0	3600.0	1800.0	2.35	7	166.0	786.0	3600.0	1800.0	2.35
8	281.0	616.0	4000.0	2100.0	2.40	8	163.0	949.0	4000.0	2100.0	2.40
9	1385.0	2001.0	5500.0	3100.0	2.60	9	1094.0	2043.0	5500.0	3100.0	2.60
10	∞	∞	5700.0	3300.0	2.70	10	∞	∞	5700.0	3300.0	2.70
NAKA						*SHIR*					
1	22.0	22.0	1000.0	200.0	1.75	1	28.0	28.0	1000.0	200.0	1.70
2	44.0	44.0	1600.0	350.0	1.85	2	29.0	57.0	1600.0	350.0	1.85
3	97.0	141.0	2000.0	650.0	1.95	3	272.0	329.0	2000.0	650.0	1.95
4	10.0	151.0	2300.0	900.0	2.05	4	10.0	339.0	2300.0	900.0	2.05
5	25.0	176.0	2600.0	1200.0	2.15	5	18.0	357.0	2600.0	1200.0	2.15
6	58.0	234.0	3200.0	1500.0	2.25	6	214.0	571.0	3200.0	1500.0	2.25
7	101.0	335.0	3600.0	1800.0	2.35	7	30.0	601.0	3600.0	1800.0	2.35
8	281.0	616.0	4000.0	2100.0	2.40	8	100.0	701.0	4000.0	2100.0	2.40
9	1385.0	2001.0	5500.0	3100.0	2.60	9	1303.0	2004.0	5500.0	3100.0	2.60
10	∞	∞	5700.0	3300.0	2.70	10	∞	∞	5700.0	3300.0	2.70
TRMA						*MYG015*					
1	5.0	5.0	1000.0	200.0	1.75	1	32.0	32.0	1000.0	200.0	1.75
2	6.0	11.0	1600.0	350.0	1.85	2	32.0	64.0	1600.0	350.0	1.85
3	55.0	66.0	2000.0	650.0	1.95	3	203.0	267.0	2000.0	650.0	1.95
4	5.0	71.0	2300.0	900.0	2.05	4	10.0	277.0	2300.0	900.0	2.05
5	6.0	77.0	2600.0	1200.0	2.15	5	25.0	302.0	2600.0	1200.0	2.15
6	178.0	255.0	3200.0	1500.0	2.25	6	243.0	545.0	3200.0	1500.0	2.25
7	2.0	257.0	3600.0	1800.0	2.35	7	54.0	599.0	3600.0	1800.0	2.35
8	217.0	474.0	4000.0	2100.0	2.40	8	123.0	722.0	4000.0	2100.0	2.40
9	27.0	501.0	5000.0	2700.0	2.50	9	1282.0	2004.0	5500.0	3100.0	2.60
10	1535.0	2036.0	5500.0	3100.0	2.60	10	∞	∞	5700.0	3300.0	2.70
11	∞	∞	5700.0	3300.0	2.70						

Validation in Sendai: comparison

Three types of inversions are conducted by using EHVRs, pEHVR, and MHVR as a target with and without a priori constraints as the initial model. The inverted underground structures can reproduce the respective HVRs in these three identification types, either with or without a priori constraints. However, the resultant velocity structures are not necessarily the same. As before, the average S-wave velocities at depths to 10, 30, and 100 m from pEHVRs and MHVRs are shown in Fig. 24 using the horizontal axis as those from EHVRs. The inversion results from pEHVR are closer to the inversion results from EHVRs than those from MHVRs. The same is true for the cases without a priori constraints, which is not shown here.

Several outliers' site codes are shown in Fig. 24. SHIR is the site with the largest difference in Vs30 and Vs100 even for the pEHVR inversion, which is the direct consequence of the poor reproduction of EHVR as seen in Fig. 19. On the other hand, NAGA shows quite good correspondence for the pEHVR inversion, while it does poor correspondence for the MHVR inversion. For Vs10, the differences are relatively small, except for ARAH by the MHVR inversion where the amplitude in the frequency range higher than 3 Hz is deficient so that soft shallow layers are eliminated.

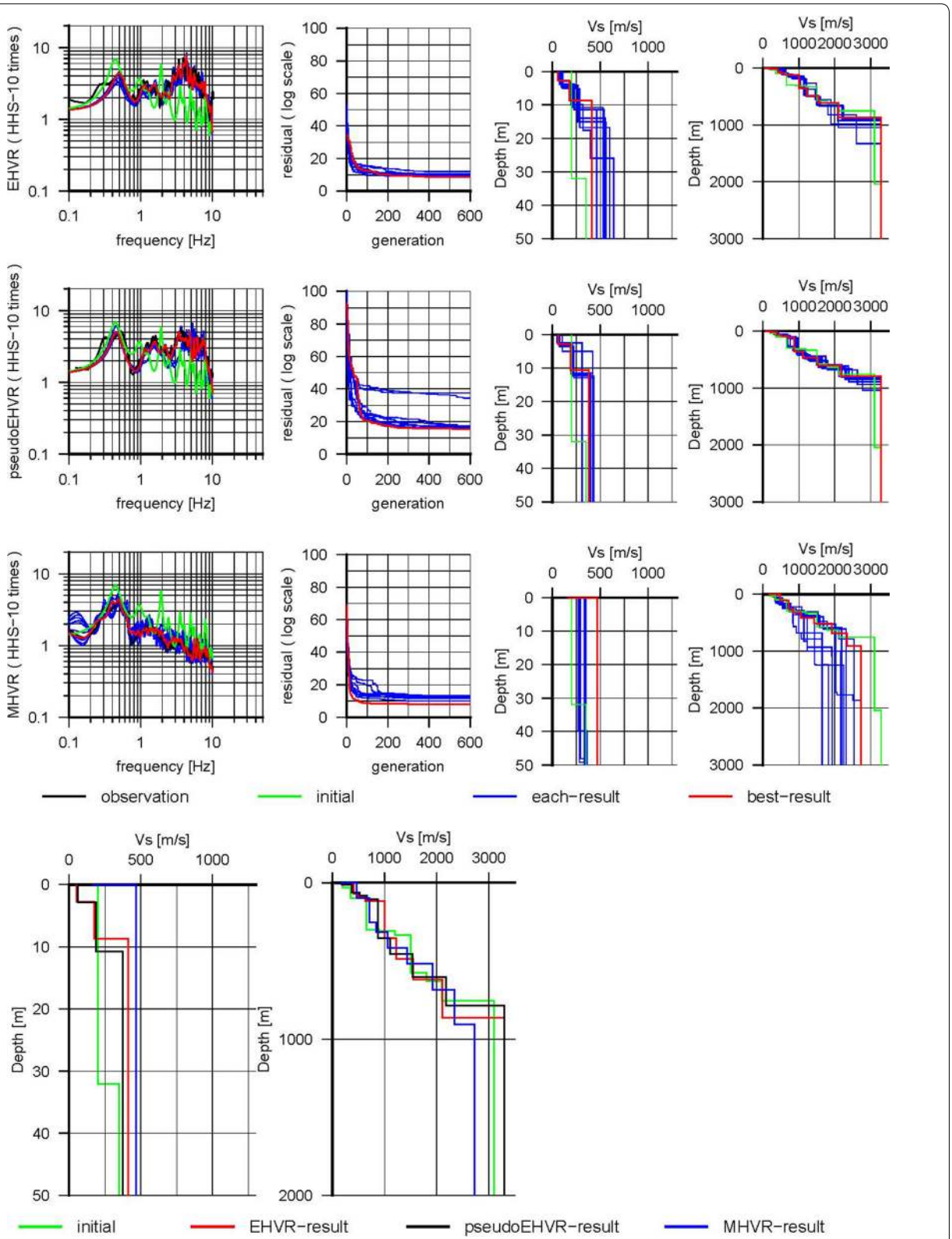

Fig. 22 Inversion results at MYG015 when an underground structure model based only on the J-SHIS information is used (i.e., no constraint in the shallow part)

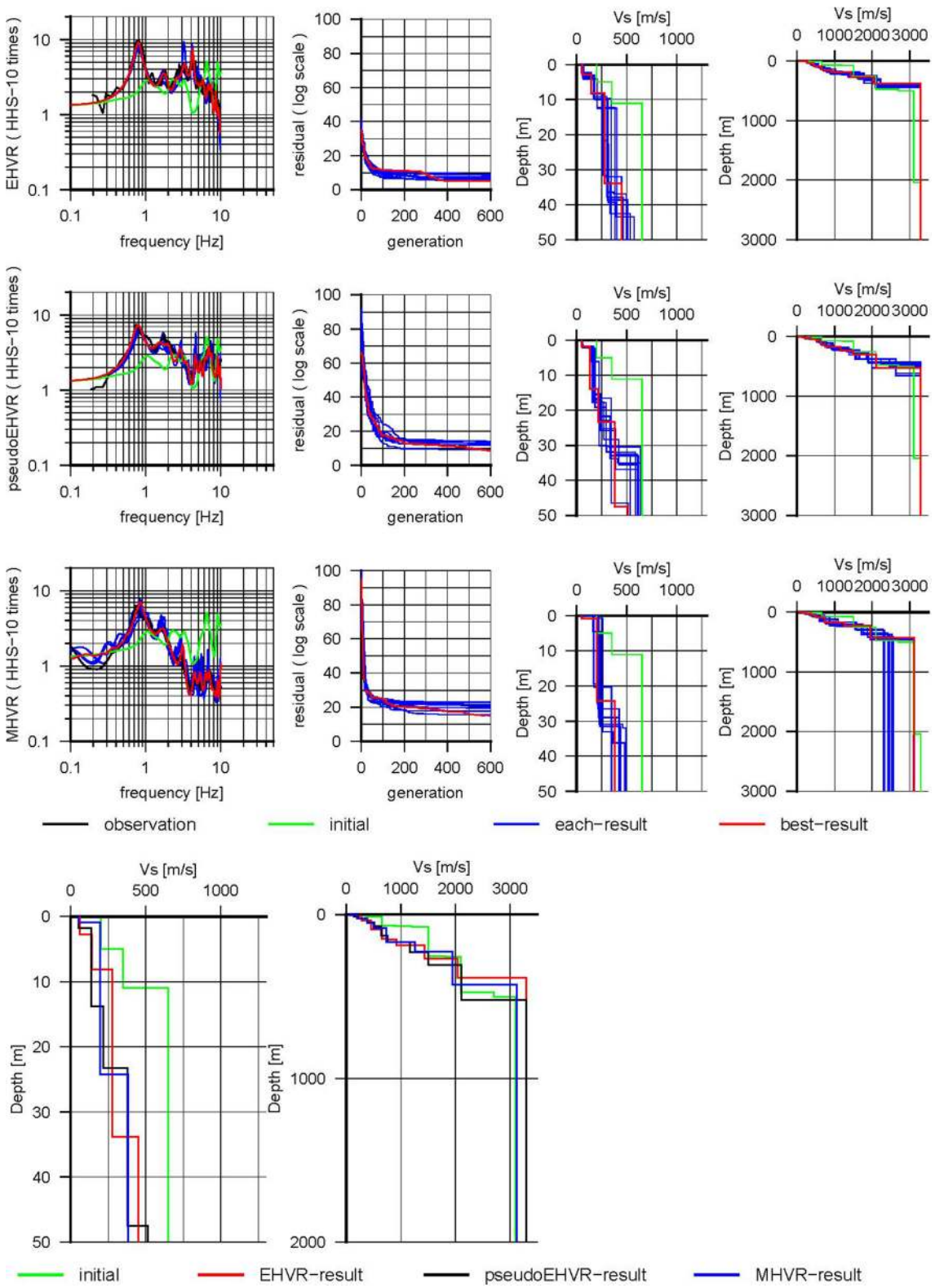

Fig. 23 Inversion results at TRMA when an underground structure model based only on the J-SHIS information is used (i.e., no constraint in the shallow part)

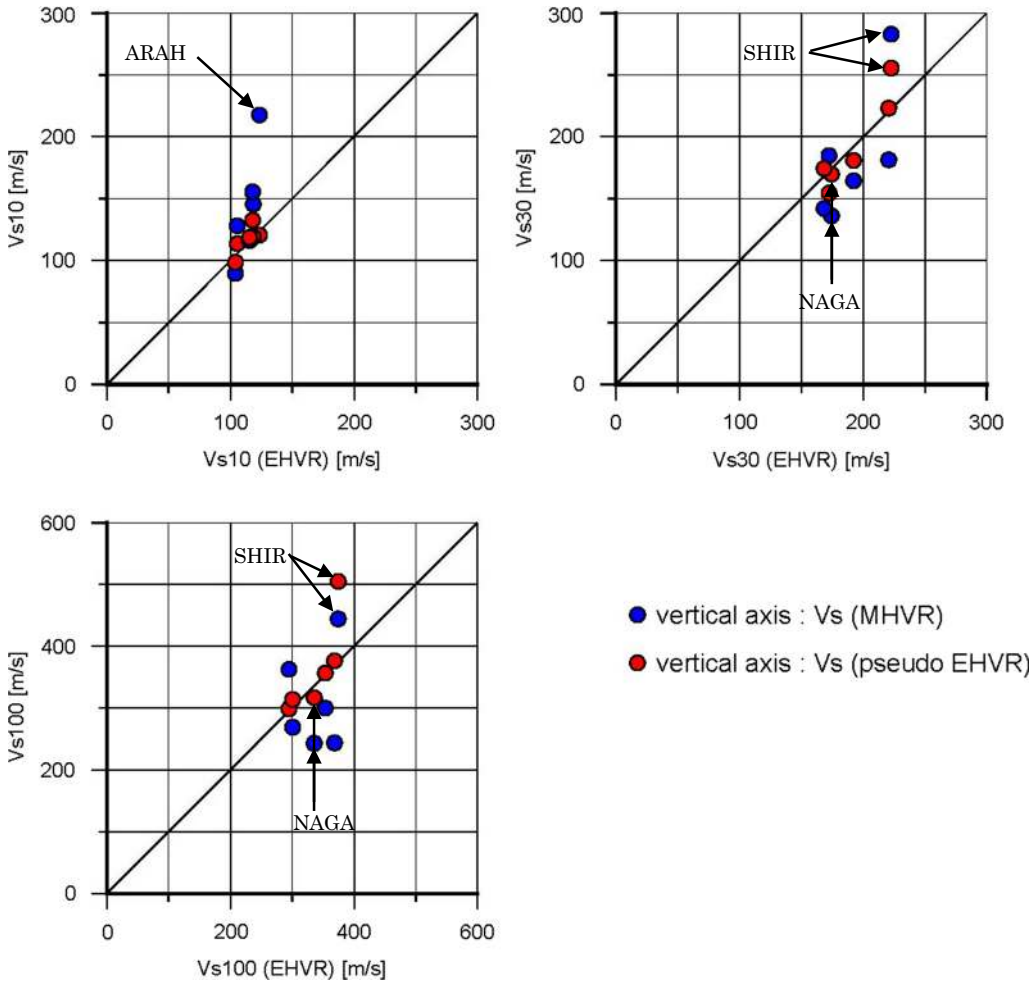

Fig. 24 Comparison of the averaged velocities from pEHVR inversion or MHVR inversion (vertical axis) with respect to those from EHVR inversion (horizontal axis). Each panel shows those for top 10, 30, and 100 m with a priori constraints. Several outliers' site codes are shown

Table 6 Comparison of the final residuals in the inversions

	ARAH	MYG015	NAGA	NAKA	SHIR	TRMA
Satoh et al. (2001) (EHVR)	61.9	57.9	231.9	72.2	93.9	78.0
Prior-model result (EHVR)	27.1 (0.0)	27.3 (0.0)	94.6 (0.0)	26.4 (0.0)	33.9 (0.0)	20.7 (0.0)
Prior-model result (pseudo-EHVR)	12.1 (21.5)	33.9 (9.0)	186.9 (23.4)	85.3 (31.3)	153.6 (48.7)	20.5 (24.0)
Prior-model result (MHVR)	11.0 (57.5)	55.1 (75.1)	68.2 (81.3)	21.4 (33.7)	32.8 (49.4)	37.7 (121.6)
J-SHIS-model result (EHVR)	23.2 (22.8)	8.7 (9.5)	7.5 (36.5)	6.0 (7.5)	12.8 (5.8)	5.2 (5.2)
J-SHIS-model result (pseudo-EHVR)	8.1 (33.4)	15.4 (15.4)	60.1 (68.7)	61.3 (34.0)	116.7 (54.0)	8.7 (25.2)
J-SHIS-model result (MHVR)	7.4 (58.5)	7.9 (105.7)	24.5 (68.1)	14.2 (42.7)	9.6 (41.4)	15.2 (111.4)

These results corroborate the two findings in the previous sections, namely "the underground structure inverted directly from MHVR could lead to a different structure" and "the underground structure inverted from pEHVR could give a structure closer to the one from EHVR". Therefore, the effectiveness of the proposed method where MHVR is converted into pEHVR using empirical EMR has been demonstrated.

Finally, the residuals shown in Eq. 4 of the inverted results based on the two initial models with and without

a priori constraints are compared in Table 6. Comparing the residual of EHVR for the initial models of Satoh et al. (2001a) and the residual of inversion from EHVR with a priori information, we found that the latter is smaller and so we might expect that the latter may be closer to the actual 1D underground structure for site amplification (as far as the assumption of the theory is fulfilled). Here we assume the latter inverted result as the representative underground structure at each site for further comparisons.

We should note here that the residuals of inversions without a priori constraints (i.e., only J-SHIS model constraint) show much smaller values than those with a priori constraints. As mentioned before, this is because the searching space for the case without a priori constraints is much wider than that with a priori constraints so that the residuals were smaller. This is the case for not only EHVR but also for pEHVR and MHVR. However, the resultant velocity structure with smaller residuals is not necessarily close to the actual velocity structure. To see the source of the magic, we calculated the residual between the HVR of the representative underground structure (that is, the HVR from the inverted model from EHVR with a priori constraints) and HVRs of inverted models from EHVR, pEHVR, and MHVR without a priori constraints are calculated and shown in the parentheses in Table 6. Focusing on the residuals of inverted models using pEHVR and MHVR with respect to HVR of the representative velocity structure in the parenthesis, the residuals from pEHVR give much smaller residuals than those from MHVR. Therefore, inversion using MHVR as a substitute of EHVR yields an underground structure that reproduces MHVR well, but it does not mean that the resultant structure from MHVR is close to the actual underground structure.

Source of errors

All the good aspect of the study shown here are based on assumptions from DFC and so the validity of the method seems to depend on the diffusivity of the wave field that we are observing. Unfortunately, it is quite difficult to provide direct evidence of the diffusivity using the observed data since we cannot observe wave field under controlled condition in the real field. For example isotropic nature of energy distribution in three-dimensional space, that is equipartition of seismic energy, cannot be easily observed because of the complex site effects near the observation point (See reviews in Kawase et al. 2015).

However, all the observational reports based on DFC unanimously shows that theoretical expressions based on DFC seem to work under variety of conditions even in the case with apparent violation of diffusivity. For example, the so-called SPAC method provides reasonable values of phase velocities of surface waves for most of the cases, even when the observed wave field may not be perfectly isotropic. This means that the formula derived from DFC is quite robust in the sense that we can extract some information of the medium from the wave field where only partially diffusive nature is established.

As a final note of caution, we must mention that our inverted solution from EHVR is non-unique in nature, since we are using nonlinear inversion scheme with HHS algorithm. It is obvious that our solution is constraint only by the target EHVR (or pEHVR) and the reference structure used, together with the searching ranges from the reference structure imposed in the inversion. Thus, we need to choose these values carefully and we have to pay attention to possible range of errors due to inherent non-uniqueness of the inversion. It is non-unique in nature; however, the strength of our EHVR inversion lies in its capability to obtain both S-wave velocities and the thicknesses of the layers down to the bedrock at the same time, unlike the other methods with strong tradeoffs between them, because we use both amplitudes and peak/trough frequencies of EHVR to constrain the velocity profile.

Conclusions

In this study, we calculated the horizontal-to-vertical spectral ratios (HVR) from observed microtremors (MHVR) as well as those of observed weak earthquake ground motions (EHVR) and compared predominant peak frequencies and amplitudes at these peak frequencies of the MHVRs and EHVRs with those calculated theoretically from S-wave velocity models based on the diffuse wave concept. When we compare MHVRs and EHVRs, we found that they share similarities but have significant differences in their shapes, especially after the fundamental peak frequency in MHVRs. This is because MHVR mainly consists of surface waves so that peaks associated with higher modes would not be as prominent as that of EHVR. We first searched for better 1-D structures at each observed site by using the proposed HHS method of Nagashima et al. (2014, 2017) for observed EHVRs based on the theory from the diffuse field concept. As a result, we successfully identified a better ground structure for each observation site from the seismological bedrock to the surface.

After looking at the systematic differences in MHVRs and EHVRs, we tried to establish a new, simple method to estimate velocity structures using single-station microtremor records since it is the most cost-effective, noninvasive method to characterize site effects. To that end, we calculated EHVR-to-MHVR ratios (EMRs) at 100 K-NET and KiK-net sites in Japan to find that there are systematic difference in the observed EMRs. Using EMRs

averaged over five different categories based on the fundamental peak frequency (*f*_peak) ranges of MHVRs as a function of the normalized frequency *f*/*f*_peak, we converted MHVRs to pseudo-EHVRs by multiplying MHVRs with the average EMRs, which are found to have higher correlation with real EHVRs than MHVRs. Using these pseudo-EHVRs, we can identify velocity structures from the seismological bedrock to the surface, with much better correspondence to the true structures than the direct use of MHVRs as substitutes. Independent evidence for the effectiveness of the pseudo-EHVR approach is presented for sites in Sendai, Japan.

We should note that high-frequency EHVRs are not only controlled by the velocity structure shallower than the engineering bedrock but also by the deep basin structure because of higher mode contributions. This is a strong opposition to the idea that site effects can be modeled only by the shallower structure below a site (say, down to 30 m), if our primary concern is focused only onto the high frequency content.

What is remaining to investigate is the way to determine numbers of unknown parameters and their range of search under various practical situations where no or not plenty of a priori information exist. We also need to explore the possibility of simultaneous inversion for earthquake and microtremors data, velocity logging and microtremor data, or data on the surface and in the boreholes. For more accurate prediction of EHVR from MHVR, we need to collect further numbers of data for both MHVR and EHVR under variety of tectonic and geological conditions to propose more effective ways of categorization in EMR.

Abbreviations

DFC: diffuse field concept; EHVR: earthquake horizontal-to-vertical spectral ratio; EMR: earthquake-to-microtremor ratio of horizontal-to-vertical spectral ratio; EW: east–west; HVR: horizontal-to-vertical spectral ratio; JMA: Japan Meteorological Agency; K-NET: Kyoshin network; KiK-net: Kiban Kyoshin network; MHVR: microtremor horizontal-to-vertical spectral ratio; NIED: National Institute for Earth Science and Disaster Resilience; NS: north–south; pEHVR: pseudo-EHVR, reproduced from EMR and MHVR; RMS: root-mean-square; UD: up–down.

Authors' contributions

Field investigations were performed by HK, FN, and YM. Microtremor analysis was performed by YM and HK. YM wrote Japanese version of the initial draft through discussion with HK and FN. FN developed and provided the inversion code for EHVR. All authors contributed to editing and revising the manuscript. All authors read and approved the final manuscript.

Author details

[1] DPRI, Kyoto University, Gokasho, Uji, Japan. [2] J-Power, Chuo-ku, Tokyo, Japan.

Acknowledgements

This study is owing to various works performed under collaboration with Shinichi Matsushima at DPRI, Kyoto University, and Francisco J. Sánchez-Sesma at IdeI, UNAM and his associates. Microtremor observations at K-NET and KiK-net stations were done by students of Kawase and Matsushima laboratory from 2000 to 2016. A part of the study was supported by the JSPS Kakenhi Grant-in-Aid for Basic Research (A) No. 26242034. The open usage of K-NET and KiK-net earthquake data collected and distributed by NIED is highly appreciated. The final revision was made during the first author's stay at ISTerre, University of Grenoble Alpes on leave from DPRI, Kyoto University.

Competing interests

The authors declare that they have no competing interests.

Ethics approval and consent to participate

The authors declare that this study does not involve human subjects, human material and human data.

Publisher's Note

Received: 28 February 2017 Accepted: 19 December 2017
Published online: 02 January 2018

References

Aki K (1957) Space and time spectra of stationary stochastic waves, with special reference to microtremors. Bull Earthq Res Inst Tokyo Univ 35:415–456

Andrews DJ (1986) Objective determination of source parameters and similarity of earthquakes of different size. In: Das S, Boatwright J, Scholz CH (eds) Earthquake source mechanics. American Geophysical Union, Washington. https://doi.org/10.1029/gm037p0259

Aoi S, Obara K, Hori S, Kasahara K, Okada Y (2000) New strong-motion observation network: KiK-net. EOS Trans Am Geophys Union 81:329

Bard P-Y (1999) Microtremor measurements: a tool for site effect estimation? In: Irikura K, Kudo K, Okada H, Sasatani T (eds) Proceedings of 2nd international symposium on the effects of surface geology on seismic motion, vol 3. Balkema, Rotterdam, pp 1251–1279

Bonnefoy-Claudet S, Cotton F, Bard P-Y (2004) The nature of noise wavefield and its applications for site effects studies. A literature review. Earth Sci Rev 79:205–227

Campillo M, Paul A (2003) Long range correlations in the seismic coda. Science 299:547–549

Cho I, Tada T, Shinozaki Y (2006) Centerless circular array method: inferring phase velocities of Rayleigh waves in broad wavelength ranges using microtremor records. J Geophys Res AGU 111:B09315. https://doi.org/10.1029/2005jb004235

Claerbout JF (1968) Synthesis of a layered medium from its acoustic transmission response. Geophysics 33:264–269

Ducellier A, Kawase H, Matsushima S (2013) Validation of a new velocity structure inversion method based on horizontal-to-vertical (H/V) spectral ratios of earthquake motions in the Tohoku Area, Japan. Bull Seismol Soc Am 103:958–970

Fujiwara H, Kunugi T, Adachi S, Aoi S, Morikawa N (2007) New K-NET: development of real-time system for strong-motion observation. J Jpn Assoc Earthq Eng 7(2):2–16 **(in Japanese with English abstract)**

Fukihara K, Matsushima S, Kawase H (2015) Identification of the velocity structure model of Kyoto Basin for strong motion prediction using observed earthquake and microtremor motions. J Jpn Assoc Earthq Eng 15(6):60–76 **(in Japanese with English abstract)**

García-Jerez A, Piña-Flores J, Sánchez-Sesma FJ, Luzón F, Perton M (2016) A computer code for forward calculation and inversion of the H/V spectral ratio under the diffuse field assumption. Comput Geosci 97:67–78. https://doi.org/10.1016/j.cageo.2016.06.016

Horike M (1985) Inversion of phase velocity of long-period microtremors to the S-wave-velocity structure down to the basement in urbanized areas. J Phys Earth 33:59–96

Kawase H, Matsuo H (2004) Amplification characteristics of K-NET, KiK-net, and JMA Shindokei network sites based on the spectral inversion technique. In: 13th world conference on earthquake engineering, Vancouver, Paper No. 454

Kawase H, Sánchez-Sesma FJ, Matsushima S (2011) The optimal use of horizontal-to-vertical (H/V) spectral ratios of earthquake motions for velocity structure inversions based on diffuse field theory for plane waves. Bull Seismol Soc Am 101:2001–2014. https://doi.org/10.1785/0120100263

Kawase H, Matsushima S, Satoh T, Sánchez-Sesma FJ (2015) Applicability of theoretical horizontal-to-vertical ratio of microtremors based on the diffuse field concept to previously observed data. Bull Seismol Soc Am 105:3092–3103. https://doi.org/10.1785/0120150134

Kinoshita S (1998) Kyoshin Net (K-Net). Seismol Res Lett 69:309–334

Lontsi AM, Sánchez-Sesma FJ, Molina-Villegas JC, Ohrnberger M, Krüger F (2015) Full microtremor H/V(z, f) inversion for shallow subsurface characterization. Geophys J Int 202:298–312. https://doi.org/10.1093/gji/ggv132

Margerin L, Campillo M, Tiggelen BV, Hennino R (2009) Energy partition of seismic coda waves in layered media: theory and application to Pinyon Flats Observatory. Geophys J Int 177:571–585. https://doi.org/10.1111/j.1365-246X.2008.04068.x

Matsushima S, Hirokawa T, De Martin F, Kawase H, Sánchez-Sesma FJ (2014) The effect of lateral heterogeneity on horizontal-to-vertical spectral ratio of microtremors inferred from observation and synthetics. Bull Seismol Soc Am 104:381–393. https://doi.org/10.1785/0120120321

Nagashima F, Matsushima S, Kawase H, Sánchez-Sesma FJ, Hayakawa T, Satoh T, Oshima M (2014) Application of horizontal-to-vertical (H/V) spectral ratios of earthquake ground motions to identify subsurface structures at and around the K-NET site in Tohoku, Japan. Bull Seismol Soc Am 104:2288–2302. https://doi.org/10.1785/0120130219

Nagashima F, Kawase H, Matsushima S (2017) Estimation of horizontal seismic bedrock motion from vertical surface motion based on horizontal-to-vertical spectral ratios of earthquake motions. In: 16th world conference on earthquake engineering, No. 3685, 9–13 Jan 2017, Santiago

Nakamura Y (1989) A method for dynamic characteristics estimation of subsurface using microtremor on the ground surface. Railw Tech Res Inst Q Rep 30(1):25–30

Nakano K, Matsushima S, Kawase H (2015) Statistical properties of strong ground motions from the generalized spectral inversion of data observed by K-NET, KiK-net, and the JMA Shindokei Network in Japan. Bull Seismol Soc Am 105:2662–2680. https://doi.org/10.1785/0120140349

Okada H (2003) The microtremor survey method. Geophysical Monograph Series No. 12 (Volume Editor: MW Asten). Society of Exploration Geophysicists, Tulsa

Okada Y, Kasahara K, Hori S, Obara K, Sekiguchi S, Fujiwara H, Yamamoto A (2004) Recent progress of seismic observation networks in Japan—Hi-net, F-net, K-NET and KiK-net. Earth Planets Space 56:xv–xviii. https://doi.org/10.1186/BF03353076

Picozzi M, Strollo A, Parolai S, Durukal E, Özel O, Karabulut S, Zschau J, Erdik M (2009) Site characterization by seismic noise in Istanbul, Turkey. Soil Dyn Earthq Eng 29(3):469–482

Prieto GA, Lawrence JF, Beroza GC (2009) Anelastic Earth structure from the coherency of the ambient seismic field. J Geophys Res Am Geophys Union 114:B07303. https://doi.org/10.1029/2008JB006067

Salinas V, Luzon F, García-Jerez A, Sánchez-Sesma FJ, Kawase H, Matsushima S, Suarez M, Cuellar A, Campillo M (2014) Using diffuse field theory to interpret the H/V spectral ratio from earthquake records in Cibeles seismic station, Mexico City. Bull Seismol Soc Am 104:995–1001. https://doi.org/10.1785/01201302

Sánchez-Sesma FJ, Rodríguez M, Iturrarán-Viveros U, Luzón F, Campillo M, Margerin L, García-Jerez A, Suarez M, Santoyo MA, Rodríguez-Castellanos A (2011) A theory for microtremor H/V spectral ratio: application for a layered medium. Geophys J Int Exp Lett 186:221–225. https://doi.org/10.1111/j.1365-246X.2011.05064.x

Satoh T, Kawase H, Matsushima S (2001a) Estimation of S-wave velocity structures in and around the Sendai Basin, Japan, using array records of microtremors. Bull Seismol Soc Am 91:206–218

Satoh T, Kawase H, Sato T (1997) Statistical spectral model of earthquakes in the eastern Tohoku district, Japan based on the surface and borehole records observed in Sendai. Bull Seismol Soc Am 87:446–462

Satoh T, Kawase H, Matsushima S (2001b) Differences between site characteristics obtained from microtremors, S-waves, P-waves and codas. Bull Seismol Soc Am 91:313–334

Steidl JH, Tumarkin AG, Archuleta RJ (1996) What is a reference site? Bull Seismol Soc Am 86:1733–1748

Stephenson WJ, Hartzell S, Frankel AD, Asten M, Carver DL, Kim WY (2009) Site characterization for urban seismic hazards in lower Manhattan, New York City, from microtremor array analysis. Geophys Res Lett Am Geophys Union 36:L03301. https://doi.org/10.1029/2008GL036444

Tada T, Cho I, Shinozaki Y (2007) Beyond the SPAC method: exploiting the wealth of circular-array methods for microtremor exploration. Bull Seismol Soc Am 97:2080–2095. https://doi.org/10.1785/0120070058

Yamanaka H (2007) Inversion of surface wave phase velocity using hybrid heuristic search method. BUTSURI-TANSA 60:265–275 **(in Japanese with English abstract)**